Surfaces and Interfaces 56 (2025) 105536

Contents lists available at ScienceDirect

Surfaces and Interfaces

journal homepage: www.sciencedirect.com/journal/surfaces-and-interfaces

Synergistic effects of hybrid CuS@$Ti_3C_2T_x$/MXene material for enhanced super capacitive energy storage and efficient water splitting

Ayesha Irfan [a], Inaam Ullah [a], Mai Li [a,*], Wendong Xu [a], Zibo Dong [a], Hanxue Zhao [a], Haotian Hu [a], Nimra Irshad [a], Kaishuai Yang [b], Ping Zhong [a,*], Paul K. Chu [c]

[a] College of Science, Donghua University, Shanghai 201620, China
[b] School of Electronic and Information Engineering, Changshu Institute of Technology, Suzhou 215000, China
[c] Department of Physics, Department of Materials Science and Engineering and Department of Biomedical Engineering, City University of Hong Kong, Tat Chee Avenue, Kowloon, Hong Kong, China

ARTICLE INFO

Keywords:
2D materials
Energy storage
Synergistic effects
Copper sulfide
Asymmetric supercapacitor
Water splitting

ABSTRACT

Two-dimensional (2D) materials, such as MXene with its 2D structure and excellent conductivity, have emerged as crucial components in electrochemistry for energy storage and water electrolysis. However, the limited capacitance exhibited by 2D MXene as a cathode material hinders widespread practical applications. In this study, CuS@$Ti_3C_2T_x$/MXene nanocomposites are synthesized by integrating copper sulfide (CuS) into $Ti_3C_2T_x$ layers to enhance energy storage characteristics alongside water-splitting properties, including the hydrogen evolution reaction (HER) and oxygen evolution reaction (OER). This remarkable progress is attributed to the synergistic effect of $Ti_3C_2T_x$ nanosheets and CuS nanoparticles (NPs), which reduce agglomeration, modulate side reactions and enhance the electron transfer rate. Cyclic voltammetry (CV) and galvanostatic charging and discharging (GCD) confirm the superior electrochemical properties of CuS@$Ti_3C_2T_x$ compared to CuS and $Ti_3C_2T_x$ alone. CuS@$Ti_3C_2T_x$ demonstrates a specific capacitance of 957.36 F g^{-1} at 1 A g^{-1}, with 99.1 % capacity retention after 10,000 cycles and a pseudo-capacitance ratio of 90.3 % at 50 mV s^{-1}. The asymmetric supercapacitor (ASC) comprising CuS@$Ti_3C_2T_x$ as the positive electrode and activated carbon (AC) as the negative electrode exhibits a specific capacitance of 361.1 F g^{-1}, 98.84 % capacity retention after 10,000 cycles and an energy density of 36.11 W kg^{-1}. CuS@$Ti_3C_2T_x$ shows a minimum overpotential of 89.7 mV in HER and 171 mV in OER. These results suggest that 2D MXene-based CuS NPs are promising for energy storage and water splitting.

1. Introduction

As the demand for innovative and efficient clean energy solutions continues to rise, the development of environmentally friendly, effective, and stable strategies for energy storage, transfer, and generation becomes increasingly crucial [1–3]. In this context, supercapacitors have emerged as a promising technology due to their outstanding durability, flexible temperature tolerance, high power output, and eco-friendliness. However, despite advancements in nanotechnology, commercially available supercapacitors utilizing carbon materials as electrodes still exhibit limited energy densities of 4, 5 Wh kg^{-1} at power densities of 10–20 kW kg^{-1}, positioning them between batteries and dielectric capacitors [4,5]. To bridge this performance gap, significant research efforts have focused on the advancement of electrode materials that exhibit high specific capacitance, energy density, and cyclic stability. A critical aspect of these developments lies in harnessing advances in surface and interface science. By optimizing the interactions between electrode materials and electrolytes at the nanoscale, researchers aim to enhance energy storage mechanisms, increase charge transfer efficiency, and improve overall device safety and longevity. These interface modifications not only influence the electrochemical properties of the materials but also contribute significantly to the overall performance of supercapacitors. Therefore, exploring innovative materials and synthesis techniques that harness these surface phenomena is vital for the future of energy storage technologies [6–8].

Materials like transition metal sulfides/oxides, conductive polymers and carbon-based substances are theoretically promising as pseudocapacitive electrodes but often face practical limitations such as reduced cycle life, poor conductivity and suboptimal capacitance, hindering their use in high-energy-density SCs [9,10]. Copper sulfide (CuS), as a

* Corresponding authors.
E-mail addresses: limai@dhu.edu.cn (M. Li), pzhong937@dhu.edu.cn (P. Zhong).

https://doi.org/10.1016/j.surfin.2024.105536
Received 20 August 2024; Received in revised form 15 November 2024; Accepted 27 November 2024
Available online 28 November 2024

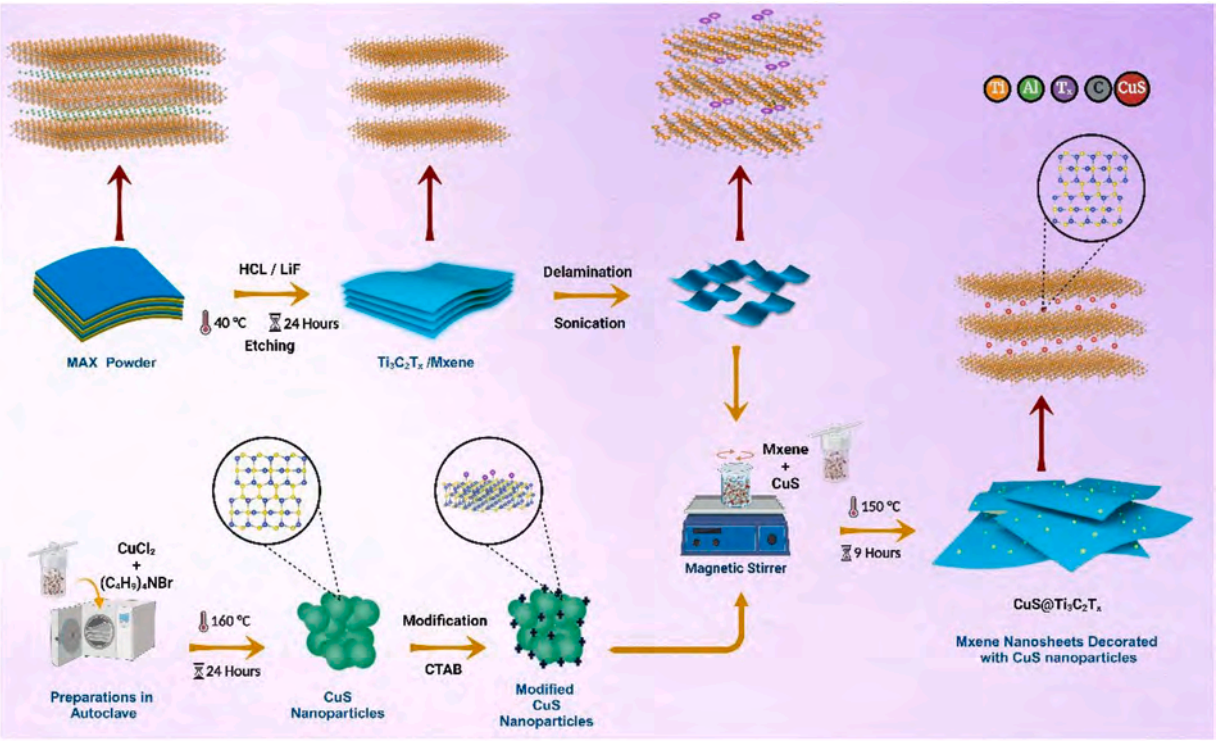

Fig. 1. Schematic illustration showing the synthesis of CuS NPs, $Ti_3C_2T_x$/MXene nanosheets, and CuS@$Ti_3C_2T_x$ nanocomposite.

transition metal sulfide, has been studied as a battery-type electrode material for asymmetric supercapacitors (ASCs) due to its ease of fabrication, high theoretical capacitance, tunable surface structure, affordability and high redox activity [11,12]. CuS-based electrode materials can be readily fabricated into a variety of micro/nanostructures, including CuS nanosheets [13], nanotubes [14], nanocages [15], micro flowers [16], nanospheres [17] and so on. Y. Liu et al. reported that hollow CuS flowers achieved a high capacitance of 536.7 F g^{-1} at a current density of 8 A g^{-1}, with 83.6 % retention after 20,000 cycles at 5 A g^{-1} [18]. Similarly, S. I. El-Hout et al. found that CuS nanospheres anchored on 7 % rGO (CuS/7 %rGO) exhibited a specific capacity of 235 C g^{-1} at 1 A g^{-1} and 95 % retention after 2000 cycles at 10 A g^{-1} [19]. However, the specific capacities of these CuS nanostructures often fall short of expectations due to the inferior structural stability and electron transfer efficiency [20]. To overcome these limitations, integrating active materials with conductive materials, such as MXene, carbon materials, metal particles and conductive polymers, has emerged as an effective strategy for CuS-based electrodes [21].

MXene is a 2D material derived from layered MAX precursors, capable of forming a graphene-like layered structure [22]. MXene nanosheets, with the general formula $M_{n+1}X_nT_x$, consist of transition metals (M) like titanium, vanadium, chromium, or molybdenum combined with carbon and/or nitrogen (X). The surface terminations (Tx) can include -O, -OH, -F, -Cl, or -Br. Their high electrical conductivity, large surface area, remarkable hydrophilicity, low work function and tunable surface chemistry make MXene attractive as supercapacitor electrodes and electrocatalysts [23–25]. Although >30 distinct stoichiometric MXene types have been synthesized, $Ti_3C_2T_x$ remains the most common for supercapacitors due to its high electrical conductivity (up to 6500 S cm^{-1}) and theoretical gravimetric capacitance (1116 F g^{-1}) [26,27]. Few-layered MXene/$Ti_3C_2T_x$ materials exhibit exceptional properties for energy storage applications, including high electrical conductivity, low ion diffusion barriers, abundant exposed active sites, and significant specific capacitance [28,29]. However, these materials face challenges such as aggregation and restacking due to strong van der Waals interactions between adjacent layers, as well as a propensity for rapid oxidation, which can adversely affect their performance [30]. To overcome these limitations, researchers have explored the combination of MXenes with other active materials to harness synergistic effects in heterojunction electrodes or catalysts [31,32]. This approach involves integrating nanomaterials into the surface and interlayers of MXene, effectively addressing the issues of stacking and oxidation while also improving conductivity and reducing the tendency for aggregation [33]. For example, Fu et al. examined few-layered MXene nanosheets wrapped in a sisal-like $NiCo_2S_4$ structure, achieving a specific capacity of 1028 C g^{-1} at 1 A g^{-1} and 94.27 % retention after 5000 cycles [34]. Zhang et al. grew CoS nanowires on few-layered $Ti_3C_2T_x$ sheets, resulting in a capacity of 528 F g^{-1} at 1 A g^{-1} and 99.3 % retention after 20,000 cycles at 10 A g^{-1} [35]. Therefore, combining CuS nanocrystals with $Ti_3C_2T_x$ nanosheets can enhance charge transfer and structural stability.

Electrocatalytic water decomposition involves two half-reactions: HER and OER. Compared to HER, which involves a two-electron transfer process, OER is more complex, involving a coupling of four electrons and protons, making it the rate-determining step in water splitting [36–39]. Currently, precious metal electrocatalysts such as iridium (Ir) and platinum-based (Pt) catalysts dominate OER and HER due to their excellent catalytic activity under alkaline conditions [40,41]. However, their scarcity and high-cost limit on large-scale applications, highlighting the urgent need for more effective and economical electrocatalysts [39,42–44]. Many materials exhibit slow kinetics for both OER and HER due to low desorption/adsorption rates of reactants [45,46]. MXene, with its unique structure, incorporates various metal and non-metal atoms during preparation, altering electronic properties and enhancing catalytic activity. In particular, CuS@$Ti_3C_2T_x$ contains numerous intrinsic defects, such as atomic vacancies and structural distortions, creating additional catalytic sites [47,48]. Bilal et al. studied the characteristics of the OER and HER of CuS/$Ti_2C_2Cl_2$ on a nickel substrate in 1 M KOH. The electrode exhibits a HER overpotential of 163 mV at 10 mA cm^{-2} and an OER overpotential of 334 mV at 50 mA cm^{-2} [49]. The convergence of nanotechnology and material science has ushered in significant advancements in surface and interface science, pivotal for enhancing the performance of energy storage devices. The

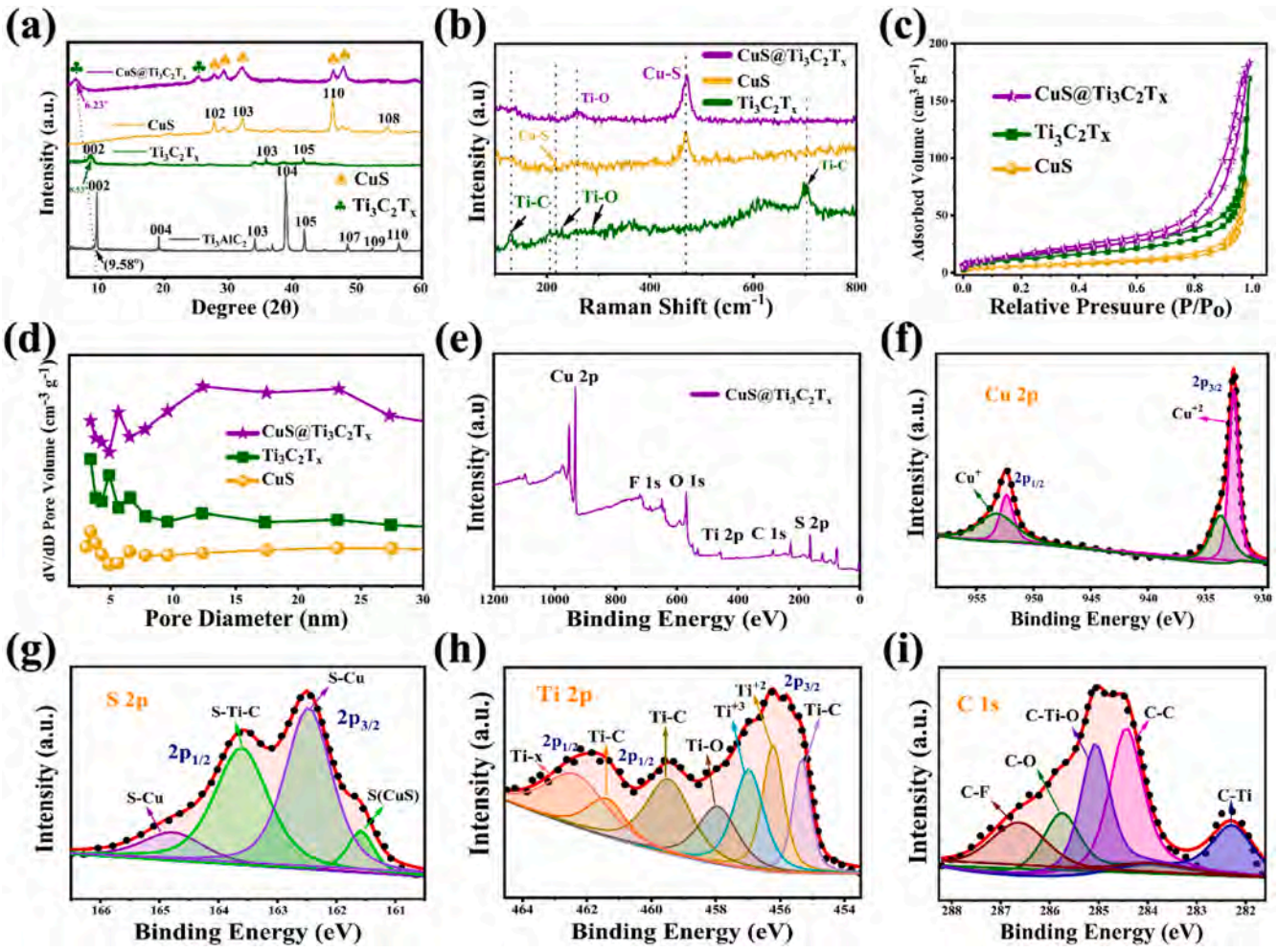

Fig. 2. (a) XRD spectra of Ti_3AlC_2, $Ti_3C_2T_x$, CuS and CuS@$Ti_3C_2T_x$; (b) Raman scattering spectra; (c) BET of synthesized samples (d) Pore size distribution curves (e) XPS spectra of (e) Full spectra (f) Cu 2p (g) S 2p (h) Ti 2p and (i) C 1 s.

interface between active materials and conductive substrates plays a critical role in optimizing charge transfer and overall device efficiency. Recent strategies in nanomaterial synthesis have emphasized modifying these interfaces to improve conductivity, stability, and electrochemical performance.

In this context, we developed a novel in situ growth strategy for synthesizing CTAB-treated CuS NPs embedded in $Ti_3C_2T_x$ using a rotating hydrothermal method, as depicted in Fig. 1. This method not only yields a well-defined porous 3D network but also significantly enhances electrolyte transport through increased interlayer spacing. Such structural modifications counteract the challenges of self-stacking in $Ti_3C_2T_x$ and agglomeration of CuS, which are crucial for maintaining high electrode stability and conductivity.

Furthermore, the advancements in surface and interface engineering like targeted modifications at the nanoscale allow for improved interactions at the electrode-electrolyte interface. For instance, DFT calculations were employed to examine the electronic structure and adsorption energies of ions on the newly formed interfaces, elucidating how these modifications can enhance electrode performance.

To demonstrate the commercial viability of our synthesized materials, we tested the electric performance of the CuS@$Ti_3C_2T_x$//AC-ASC configuration, achieving a specific capacitance of 361.1 F g^{-1} and an impressive capacity retention of 98.84 % after 10,000 cycles, alongside an energy density of 36.11 W kg^{-1}. Additionally, our composite electrode exhibited superior electrocatalytic properties in hydrogen evolution and oxygen evolution reactions, with minimal overpotentials and favorable Tafel slopes, illustrating the tangible benefits of our approach.

These results emphasize the potential of CuS@$Ti_3C_2T_x$ in advancing renewable energy applications by leveraging innovations in surface and interface science, thereby paving the way for more efficient and stable energy storage solutions in the future.

2. Experimental section

2.1. Material preparation

Lithium fluoride (LiF, 99.9 %), MAX powder (Ti_3AlC_2, 99 %), polyvinylpyrrolidone (PVP, 99 %), copper chloride ($CuCl_2$), hydrochloric acid (HCl) and tetrabutylammonium bromide ($(C_4H_9)_4NBr$) were sourced from Sinopharm Chemical Reagent Co., Ltd, as well as sodium sulfide (Na_2S) and ascorbic acid ($C_6H_8O_6$) from Shanghai Macklin Biochemical Co., Ltd. All chemicals used in this study were of analytical grade and used without further purification. These chemicals were dissolved in deionized (D.I.) water to prepare the required solutions.

2.1.1. Preparation of $Ti_3C_2T_x$/MXene

For the synthesis of multilayer $Ti_3C_2T_x$/MXene, the etching solution was prepared using 40 ml HCL and 2 g of LiF. The mixture was stirred for half an hour at 40 °C and then the 2 g of Ti_3AlC_2/MAX powder was added slowly to the etching solution. The etching solution was then stirred for 1 day at around 40 °C in the water bath. The solution was centrifuged at 4200 rpm for half an hour. The solution was then washed

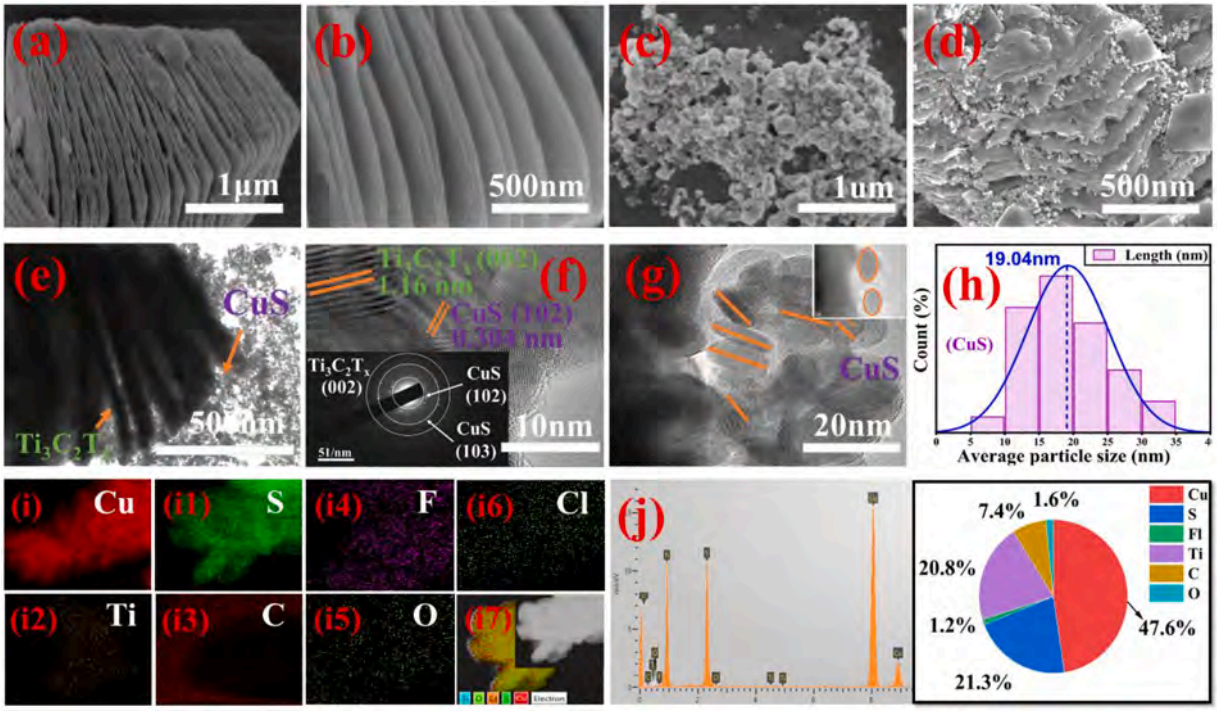

Fig. 3. Morphology and EDS results; SEM images of; (a, b) $Ti_3C_2T_x$, (c) CuS, and (d) CuS@$Ti_3C_2T_x$; (e) TEM image of CuS@$Ti_3C_2T_x$; (f) HR-TEM image of CuS@-$Ti_3C_2T_x$ with the inset showing the SAED pattern; (g, h) Particle size of CuS and calculated average particle size; (i-i7) EDS elemental maps of CuS@$Ti_3C_2T_x$; (j) Elemental concentrations determined by EDS.

with ethanol and DI water for several times until pH~7. The resultant solution was vacuum filtered to obtain a film, which was then mixed with DI water and make it to around 150 ml. The solution was exposed to Argon gas and then sonicated in an ice bath for 1 h. The sonicated mixture was centrifuged for 1 h to yield multilayer $Ti_3C_2T_x$. The solution was poured into petri dishes, pre-frozen for 6 h at −32 °C, and then freeze dried at −64 °C for 12 h to obtain the freeze-dried $Ti_3C_2T_x$/MXene powder.

2.1.2. Synthesis of CuS

CuS NPs were successfully synthesized in a two-step process in an aqueous solution, providing precise control over the formation and ensuring high-quality NPs. In the first step, a carefully measured solution was prepared by combining deionized water, polyvinylpyrrolidone (PVP), $CuCl_2$ solution and $(C_4H_9)_4NBr$ solution. This solution was then stirred, resulting in the formation of turbidity. To initiate the synthesis, an ascorbic acid solution was added and the mixture was stirred for a 2 h. In the second step, the Na_2S solution was added slowly to the prepared solution while stirring and left undisturbed at room temperature. During this process the solution turned to brown color indicating the formation of Cu_2S hollow spheres. To enhance the synthesis process, the brownish mixture was transferred to an autoclave lined with polytetrafluoroethylene (PTFE) and heated at a controlled temperature for 24 h. This controlled heating process facilitated the transformation of Cu_2S into well-crystallized CuS NPs, ensuring the desired structural properties. After synthesis, the CuS solution was centrifuged, washed with DI water and ethanol to remove impurities and dried in air. The resulting CuS NPs were then ready for further analysis and applications.

2.1.3. Synthesis of CuS@$Ti_3C_2T_x$/MXene

CuS@$Ti_3C_2T_x$/MXene was fabricated using a solvothermal method. Specifically, 0.3 g of CuS NPs and 0.2 g of $Ti_3C_2T_x$/MXene powder were mixed in 60 mL of ethylene glycol. After stirring the mixture magnetically for 30 min, 0.1 mL of hydrazine hydrate (N_2H_4) was slowly added and the mixture was stirred until a homogeneous solution was obtained. This mixture was then transferred to a stainless-steel autoclave and heated at 150 °C for 9 h. The resulting material was separated by centrifugation, washed and centrifuged again at 4500 rpm several times, followed by drying under vacuum at 85 °C for 9 h. To enhance the robustness of our results, we conducted all experiments for each of the three samples (CuS, $Ti_3C_2T_x$ and CuS@$Ti_3C_2T_x$) with five replicates, systematically testing their electrochemical performance to ensure reliability and reproducibility.

3. Results and discussion

The preparation process and schematic structure of $Ti_3C_2T_x$, CuS and CuS@$Ti_3C_2T_x$ are shown in Fig. 1 and electrode formation is described in Supporting Section S1. The synthesized materials and electrodes are systematically characterized and thoroughly discussed in Supporting Section S2.

Fig. 2 shows the XRD, Raman spectroscopy and XPS results of $Ti_3C_2T_x$, CuS and CuS@$Ti_3C_2T_x$. According to Fig. 2a, Ti_3AlC_2 (MAX precursor) shows diffraction peaks at 2θ = 9.58°, 19.2°, 34.2°, 36.81°, 38.81°, 41.65°, 48.45°, 52.4° and 56.31° corresponding to Miller indices (002), (004), (101), (103), (104), (105), (107), (109) and (110) respectively, (as referenced by JCPDS # 52–0875 for $Ti_3C_2T_x$ and JCPDS # 32–1383 for TiC) [50]. XRD reveals a significant shift in the peak from 9.58° to 8.53° for $Ti_3C_2T_x$, associated with the (002) plane and the disappearing peak at 38.81° corresponds to the (103) plane showcasing that Al layers have been successfully eliminated [51]. Peaks at 2θ = 27.78°, 32.1°, 47.63° and 54.7° indicating a uniform crystal structure of CuS NPs, (JCPDF # 65–3588) [52]. A further peak shift is observed, with the (002) index moving from 8.53° to 6.23° due to the insertion of CuS NPs into $Ti_3C_2T_x$ nanosheets. The increase in the intensity of CuS@-$Ti_3C_2T_x$ peaks showcasing the improvement in crystal structure and the peak at 25.1° arises from TiO_2.

Fig. 2b shows two diffraction peaks at 129.44 and 701 cm^{-1} corresponding to Ti-C in $Ti_3C_2T_x$, while the smaller peaks at 129.9 and 290 cm^{-1} indicate Ti-O and O-Ti-O, respectively. The three prominent Raman

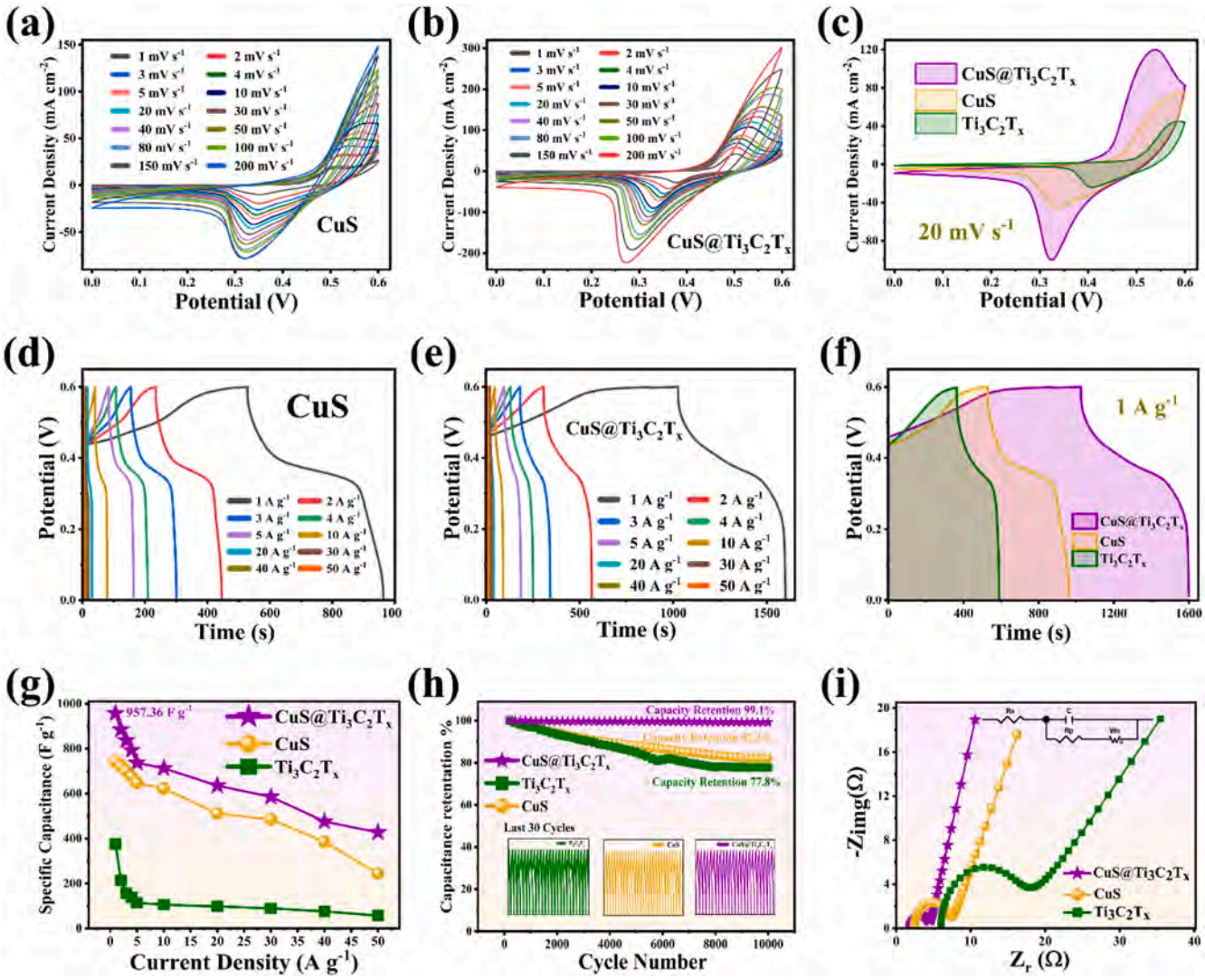

Fig. 4. CV plots of (a) CuS and (b) CuS@$Ti_3C_2T_x$; (c) CV comparison; GCD plots of (d) CuS and (e) CuS@$Ti_3C_2T_x$; (f) comparison graph; (g) Current density vs specific capacitance; (h)% capacity retention; (i) Nyquist plots for EIS.

peaks observed at 216, 468.58 and 472.32 cm^{-1} are associated with Cu-S, confirming the crystalline structure of CuS NPs. In the CuS@$Ti_3C_2T_x$ composite, similar peaks are observed, albeit with varying intensities. A notable peak shift occurs for Cu-S from 468.58 to 472.32 cm^{-1}, highlighting the strong synergistic effects between CuS and $Ti_3C_2T_x$. The disappearance of the Ti-C bond in the composite can be attributed to the interaction between CuS NPs and the $Ti_3C_2T_x$ sheets, likely inducing changes in the vibrational modes of the Ti-C bonds and altering the electronic environment within the $Ti_3C_2T_x$ structure. This interaction resulted in the suppression of characteristic peaks associated with the Ti-C bonds. Fig. 2c, d present the BET isotherms for $Ti_3C_2T_x$, CuS and CuS@$Ti_3C_2T_x$ electrode materials, revealing IV-type isotherm with an H3 hysteresis loop, indicative of their mesoporous characteristics. The specific surface area of CuS@$Ti_3C_2T_x$ is 50 m^2 g^{-1}, surpassing that of the individual $Ti_3C_2T_x$ (31.97 m^2 g^{-1}) and CuS (26.94 m^2 g^{-1}), which highlights the composite's enhanced porosity. Additionally, the pore diameter of CuS@$Ti_3C_2T_x$ is 6.18 nm, larger than that of $Ti_3C_2T_x$ (19.13 nm) and CuS (17.04 nm). This increase in surface area and pore diameter upon incorporating CuS NPs into the $Ti_3C_2T_x$ nanosheets is significant. The augmented surface area provides a greater number of active sites for electrolyte ion interaction with the electrode material, which is crucial for improving electrochemical performance. Consequently, the CuS@$Ti_3C_2T_x$ composite demonstrates significant potential for enhanced electrochemical properties in supercapacitor applications, as the increased active sites facilitate improved charge transfer and energy storage capabilities. This analysis supports the hypothesis that composite materials can leverage the strengths of individual components, leading to superior performance in energy storage technologies.

Fig. 2e presents the complete X-ray Photoelectron Spectroscopy (XPS) spectrum of CuS@$Ti_3C_2T_x$, revealing the significant presence of key elements, including Ti, C, Cu and S. Additionally, it highlights the presence of functional groups such as F and O, underscoring the material's complex chemical composition. Fig. 2f depicts the spectrum of Cu in CuS@$Ti_3C_2T_x$, showing two peaks at 952.4 and 932.5 eV for Cu^+ (Cu $2p_{1/2}$ and Cu $2p_{3/2}$, respectively). Two other peaks at 933.6 and 952.4 eV correspond to Cu^{2+}. Fig. 2g shows the S 2*p* spectrum of CuS@$Ti_3C_2T_x$, revealing peaks at 161.58, 162.4, 163.61 and 164.82 eV, attributed to S-CuS, S-Cu, S-Ti-C and S-Cu for S $2p_{3/2}$ and S $2p_{1/2}$, respectively. The presence of the Cu-S bond confirms the synthesis of uniform CuS crystals [53]. Fig. 2h shows Ti 2*p* peaks at 455.3, 456.2, 456.9, 458, 459.5 and 462.5 eV corresponding to (Ti-C, Ti^{+2}, Ti^{+3}) $2p_{3/2}$, (Ti-O, Ti-C) $2p_{1/2}$ and Ti-X, respectively [54]. Fig. 2i shows the C 1 s peaks at 282.2, 284.45, 285.1, 285.8 and 286.5 eV for C-Ti, C-C, Ti-C-O, C-O and C-F, respectively [22]. These peaks confirm the strong interactions between Ti and C in $Ti_3C_2T_x$.

SEM, TEM and HR-TEM are performed to examine the nanostructure

and morphology of $Ti_3C_2T_x$, CuS and CuS@$Ti_3C_2T_x$. Fig. 3(a, b) and S2b show the SEM images of the irregular and well-stacked nanosheet structure of $Ti_3C_2T_x$ with active sites created by etching of Al from Ti_3AlC_2 (Fig. S2a), while the HR-TEM image reveals the $Ti_3C_2T_x$ nanosheets in Fig. S2c. Fig. 3c displays the SEM image of self-agglomeration CuS NPs Fig. S3(a, b). To overcome the self-assembly of CuS NPs, it is imperative to increase the available surface area. $Ti_3C_2T_x$ nanosheets etched by HCl have active layers that can provide a large surface area by mitigating the agglomeration of these NPs. The SEM images in Figs. 3d and S4a, demonstrate that $Ti_3C_2T_x$ nanosheets have a large surface area for active material, which securely anchor their positions and show a greater number of CuS NPs sandwiched between these layers. The distinctive micro-structure of CuS@$Ti_3C_2T_x$ provides a substantial contact area for electrochemical reactions.

Fig. 3e displays the TEM image of CuS@$Ti_3C_2T_x$, revealing ultra-thin $Ti_3C_2T_x$ sheets that are instrumental in dispersing the CuS NPs. The CuS NPs are efficiently enclosed by these ultrathin $Ti_3C_2T_x$ sheets, as shown in Fig. S4b. Fig. 3f illustrates the multi-layer spacing of CuS@$Ti_3C_2T_x$. The distinct ᴅ-spacing of 1.16 nm corresponds to the (002) planes of $Ti_3C_2T_x$, whereas the 0.281 nm and 0.304 nm spacings align with the (103) and (102) planes of CuS, respectively [55]. The SAED pattern of CuS@$Ti_3C_2T_x$, reveals both CuS and $Ti_3C_2T_x$. Fig. 3g displays the TEM image of CuS, showing that they tend to self-aggregate. The $Ti_3C_2T_x$ nanosheets (averaging 40 nm) have a large surface area, but in contrast, the calculated average size of agglomeration-free CuS NPs is 19.04 nm, making them more suitable for insertion into the generated active sites between $Ti_3C_2T_x$ sheets. Fig. 3h shows the average size of CuS NPs anchored on the surface of $Ti_3C_2T_x$ measured by HR-TEM. Fig. 3(i-i6) displays the EDS results of CuS@$Ti_3C_2T_x$ showing Cu, S, Ti, C, F, Cl and O. Meanwhile, Fig. 3(i7) illustrates the elemental contributions of CuS@$Ti_3C_2T_x$ with the electron image in the inset. Fig. 3j presents the concentration of these elements involved in CuS@$Ti_3C_2T_x$. Cu and S have the highest concentration of 68.9 %, indicating that a significant portion of the $Ti_3C_2T_x$ surface is covered by CuS.

3.1. Electrochemical assessment

The electrochemical evaluation of the energy storage mechanism was conducted using a CHI660E electrochemical workstation. The working electrodes consisted of CuS, $Ti_3C_2T_x$ and CuS@$Ti_3C_2T_x$, immersed in a 1.0 M KOH electrolyte solution supplemented with 0.2 mM potassium hexacyanoferrate (II) ($K_4[Fe(CN)_6]$) as the electrolyte. A Silver/Silver Chloride (Ag/AgCl) reference electrode and a graphite plate counter electrode (10 × 10 × 3 mm) were used. The potential window of the working electrodes was established as 0 to 0.6 V. To ensure the reliability and reproducibility of our results, each experiment for the prepared electrodes (CuS@$Ti_3C_2T_x$, CuS, and $Ti_3C_2T_x$) was conducted five times, during which we assessed the electrochemical properties of each sample to verify the accuracy of our findings. Fig. S5 displays the cyclic voltammetry (CV) curves along with the corresponding error bars and standard deviations for the anodic and cathodic peaks of all electrodes. To further analyze the results, galvanostatic charge-discharge (GCD) curves were obtained for each electrode type (CuS@$Ti_3C_2T_x$, CuS, and $Ti_3C_2T_x$), with five replicates for each sample facilitating the calculation of specific capacitance and energy density represented in Fig. S6. The experiment that exhibited the closest alignment with the calculated mean values and the minimum deviation was selected for further analysis.

Fig. 4 (a, b) display the CV results for CuS and CuS@$Ti_3C_2T_x$ at various scanning rates (1 to 200 mV s^{-1}). The electrode synthesis is illustrated in Fig. S1. Sharp rise in the current density is observed for redox peaks (anodic and cathodic). The broad redox peaks of CuS@$Ti_3C_2T_x$ reflect the reversible conversion of ferrocyanide to ferricyanide, resulting in the oxidation of Cu [56]. The shape of the CV plots remains consistent across increasing scanning rates, with continuous increases in intensity and current, indicating low resistance, cyclic stability, reversibility and favorable electrochemical kinetics. However, achieving a reversible capacitive trend for the composite electrodes proves challenging due to the translational absorption behavior of CuS. CV results for NF and $Ti_3C_2T_x$, shown in Fig. S7(a, b), reveal lower current densities at scanning rates of 5, 10, 20, 30, 40 and 50 mV s^{-1}.

Fig. 4c compares the CV results of $Ti_3C_2T_x$, CuS and CuS@$Ti_3C_2T_x$. The increased area of the CV curve for CuS@$Ti_3C_2T_x$ suggests enhanced electron transfer, with sharper redox peaks indicating improved kinetics. The increasing intensities and areas of the reversible redox reactions imply valence changes of Cu^{+}/Cu^{2+}accompanied by electron transfer [57]. Fig. 4(d, e) presents the GCD curves, revealing the charging and discharging properties of CuS and CuS@$Ti_3C_2T_x$ at different current densities (1 to 50 A g^{-1}). As current density increases, the discharging time decreases, with the longest discharging time observed at a low current density of 1 A g^{-1}. This decline in discharge time at higher current densities is due to the faster movement of charge carriers, resulting in more efficient and rapid discharge of stored energy. The GCD curves for NF and $Ti_3C_2T_x$ are shown in Fig. S8(a, b). which demonstrate shorter discharge times compared to CuS and CuS@-$Ti_3C_2T_x$. Fig. 4f illustrates the charging/discharging times and a comparative graph at 1 A g^{-1}. CuS@$Ti_3C_2T_x$ has exceptional integrity and dispersion, yielding a charging/discharging time of 1599.8 s, which is significantly longer than that of CuS with a discharging time of 963.8 s. In comparison, $Ti_3C_2T_x$ has a shorter discharging time of 590.5 s. CuS@$Ti_3C_2T_x$ shows a longer discharging time than CuS, indicating a significantly higher specific capacitance for CuS@$Ti_3C_2T_x$ boding well for supercapacitors.

Fig. 4g presents the specific capacitance versus current density relationship based on GCD for CuS, $Ti_3C_2T_x$ and CuS@$Ti_3C_2T_x$ at various current densities (1 to 50 A g^{-1}). The specific capacitance of CuS is 734.49 F g^{-1} at 1 A g^{-1}, while CuS@$Ti_3C_2T_x$ achieves a larger capacitance of 957.36 F g^{-1} at the same current density.

The relationship between power density and energy density is shown in the Fig. S9. As expected, energy density decreases with increasing power density, indicating that higher power densities limit the rate at which ions can be intercalated or deintercalated in the electrode, leading to slower reaction kinetics and reduced energy storage capacity. At a power density of 300 W kg^{-1}, the CuS and $Ti_3C_2T_x$ electrodes demonstrate maximum energy densities of 37.71 Wh kg^{-1} and 19.2 Wh kg^{-1}, respectively, while CuS@$Ti_3C_2T_x$ achieves a remarkable energy density of 47.86 Wh kg^{-1}. The synergy between CuS and $Ti_3C_2T_x$ in the composite enhances overall energy storage performance.

Fig. 4h illustrates the cyclic stability of CuS and $Ti_3C_2T_x$ compared to CuS@$Ti_3C_2T_x$. The CuS@$Ti_3C_2T_x$ composite demonstrates robust cyclic stability with 99.1 % capacity retention after 10,000 cycles, whereas the CuS electrode retains only 82.2 % of its capacity. The excellent cycling stability of CuS@$Ti_3C_2T_x$ can be attributed to several factors: the strong interaction between CuS NPs and $Ti_3C_2T_x$ nanosheets enhances structural integrity during charge-discharge cycles, preventing significant physical degradation or agglomeration of CuS particles. Additionally, the layered structure of $Ti_3C_2T_x$ allows for efficient ion transport, contributing to capacity retention over extended cycling. The high surface area and conductivity of $Ti_3C_2T_x$ facilitate rapid electron transfer and ion diffusion, minimizing resistance during cycling.

The electrochemical kinetics of CuS@$Ti_3C_2T_x$, CuS and $Ti_3C_2T_x$ are investigated by EIS. The Nyquist plots in Fig. 4i reveal that CuS@$Ti_3C_2T_x$ has the smallest semicircle in the high-frequency region compared to pristine CuS and $Ti_3C_2T_x$. The fitted equivalent circuit results indicate that the calculated charge transfer resistance (R_{ct}) of CuS@$Ti_3C_2T_x$, CuS and $Ti_3C_2T_x$ are 2, 2.45 and 6 Ω, respectively. The smaller charge transfer resistance of CuS@$Ti_3C_2T_x$ implies superior electron transfer and electrical conductivity. The slope in the low-frequency region, determined by the Warburg constant (W_o), reflects the ionic conductivity. CuS@$Ti_3C_2T_x$ exhibits the steepest slope with the minimum W_o, indicating the highest ionic conductivity. The R_{ct} and W_o values are obtained by fitting the equivalent circuits of CuS@$Ti_3C_2T_x$ Fig. 4(i),

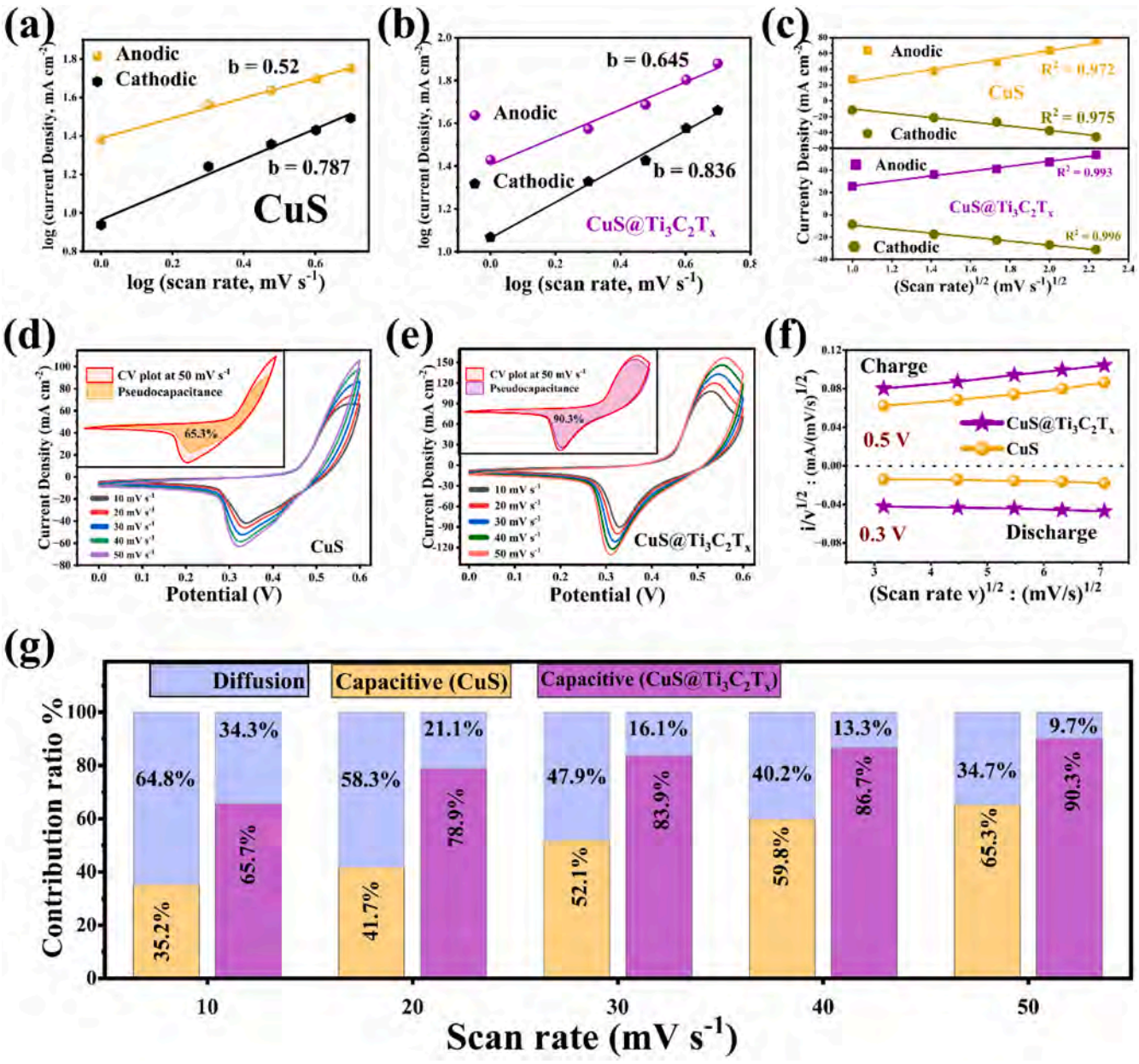

Fig. 5. b values of (a) CuS and (b) CuS@$Ti_3C_2T_x$; (c) R^2 plots of CuS and CuS@$Ti_3C_2T_x$; CV plots (10–50 mV s^{-1}) and pseudocapacitive characteristics at 50 mV s^{-1} of (d) CuS and (e) CuS@$Ti_3C_2T_x$; (f) Charging/Discharging curves of CuS and CuS@$Ti_3C_2T_x$; (g) comparison of capacitive and diffusive effects.

(Fig. S10a), CuS (Fig. S10b) and $Ti_3C_2T_x$ (Fig. S10c) along with the Bode plots.

Fig. 5 illustrates the double-layer capacitance of CuS and CuS@$Ti_3C_2T_x$, highlighting pseudo-capacitance values obtained from the CV data at various current densities. Fig. 5a, b presents the calculated anodic and cathodic b-values for the pseudocapacitive and diffusion properties of both materials. The b-values for CuS are 0.52 (anodic) and 0.787 (cathodic), indicating moderate behavior. In contrast, CuS@$Ti_3C_2T_x$ exhibits remarkable pseudocapacitive behavior with b-values of 0.645 and 0.836, respectively. The higher b-values suggest that CuS@$Ti_3C_2T_x$ has a greater charge storage capacity and superior pseudocapacitive characteristics. The slope R^2 values for CuS@$Ti_3C_2T_x$ align with the b-values, showing anodic and cathodic R^2 values of 0.993 and 0.996, respectively, as illustrated in Fig. 5c.

Fig. 5d depicts the CV of CuS, revealing distinct redox peaks at scanning rates of 10–50 mV s^{-1}. Pseudocapacitance, evaluated by Dunn's method [58] demonstrates two contributions: a surface capacitive contribution enhancing power density and a diffusion-controlled contribution improving energy density. The inset of Fig. 5d shows the primary capacitive contribution with the redox peaks, while the yellow area represents the capacitive component of pseudocapacitance at 50 mV s^{-1}, with surface-controlled behavior accounting for 65.3 % and diffusion-controlled contribution for 34.7 %.

Fig. 5e reveals a significant increase in current densities with sharp redox peaks for CuS@$Ti_3C_2T_x$. As shown in Fig. 5e inset, the escalating trend suggests that at 50 mV s^{-1}, the pseudo-capacitance ratio for the surface control capacitive contribution reaches 90.3 %. Furthermore, Fig. 5f shows the calculated slopes (k_1) at different potential values effectively describing the charging and discharging behavior for pseudocapacitance as outlined in Eq. (1).

$$\frac{i(V)}{v^{1/2}} = k_1 v^{1/2} + k_2 \quad (1)$$

The graph of $i(V)/v^{1/2}$ versus square root of scanning rate $(v)^{1/2}$:(mV

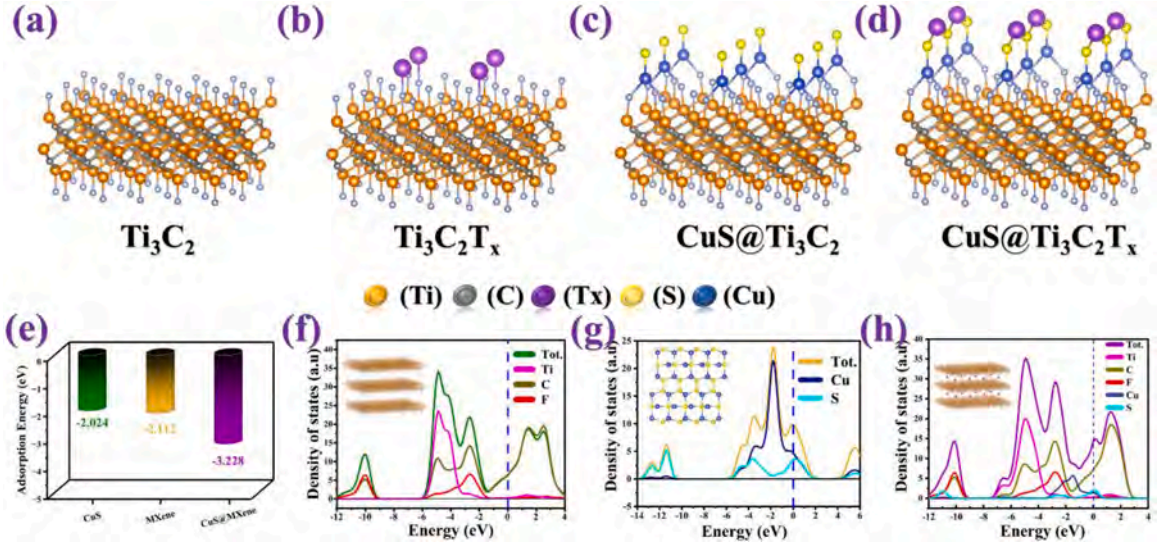

Fig. 6. Adsorption Energy (E_{ad}) models of (a) Ti_3C_2, (b) $Ti_3C_2T_x$, (c) CuS@Ti_3C_2 composite, and (d) CuS@$Ti_3C_2T_x$ composite; (e) Adsorption energies of CuS, $Ti_3C_2T_x$/MXene, and CuS@$Ti_3C_2T_x$/MXene; (f) PDOS of $Ti_3C_2T_x$; (g) PDOS of CuS; (h) PDOS of CuS@$Ti_3C_2T_x$.

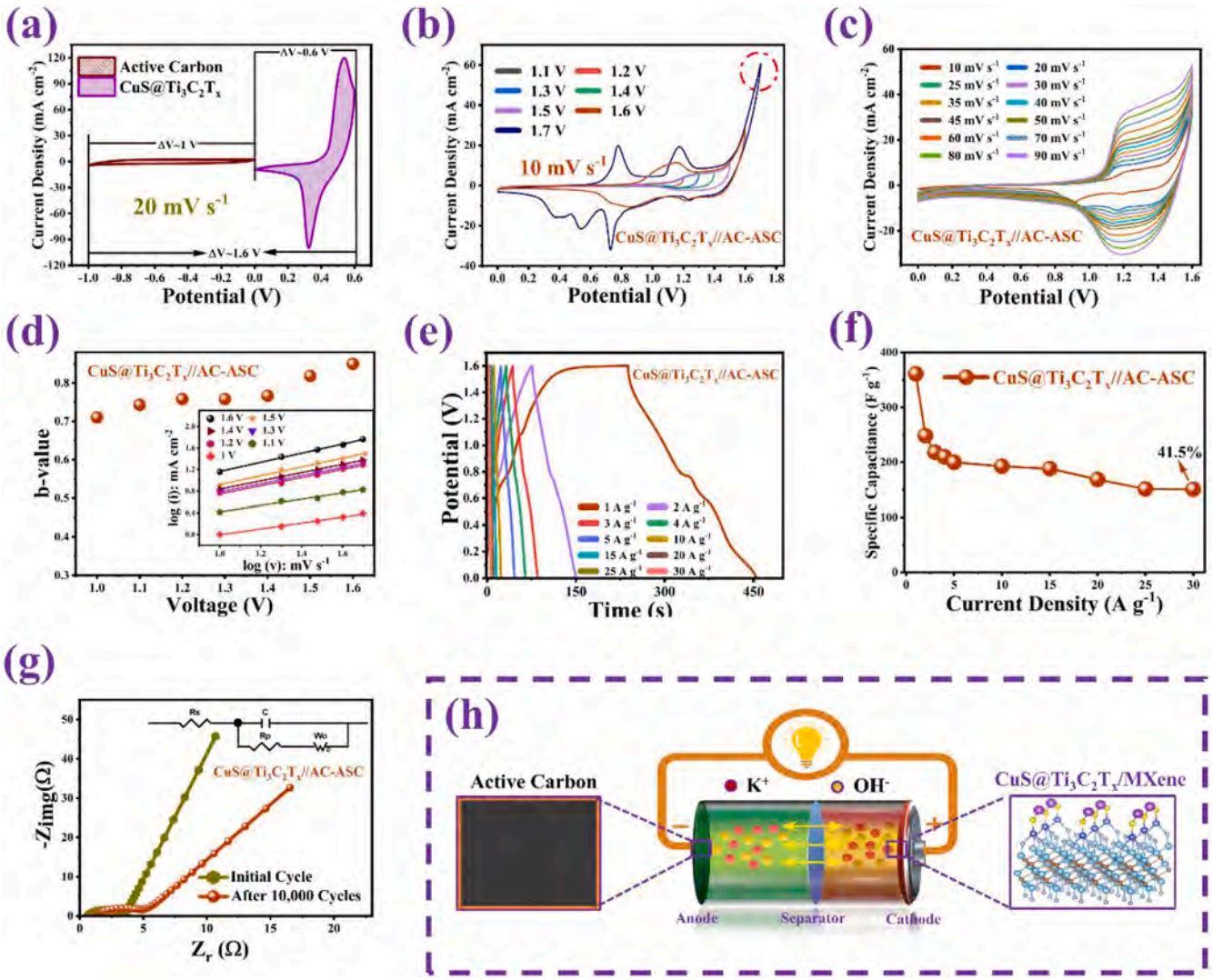

Fig. 7. (a) CV comparison between the CuS@$Ti_3C_2T_x$ anode and AC cathode; (b) CV curves in different potential windows; (c) CV curves at different current densities (1–90 mV s^{-1}); (d) b values of the device at potentials from 1 to 1.7 V; (e) GCD curves at different current densities in the potential window of 0–1.6 V; (f) Specific capacitances calculated at various current densities; (g) Nyquist plot of CuS@$Ti_3C_2T_x$//AC-ASC; (h) Schematic illustration of CuS@$Ti_3C_2T_x$//AC-ASC.

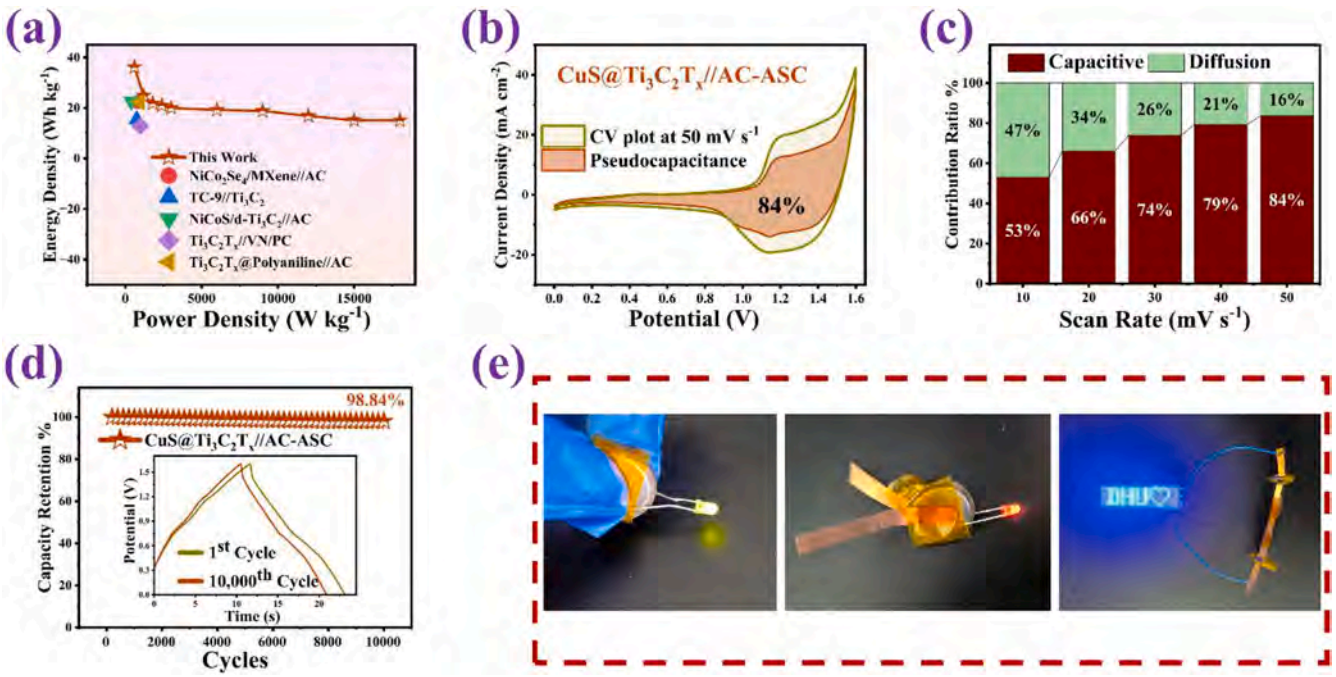

Fig. 8. (a) Ragone plot of CuS@$Ti_3C_2T_x$//AC-ASC and comparison with similar devices in the literature; (b) Pseudo-capacitance at 50 mV s^{-1}; (c) Capacitive and diffusion contributions at various scanning rates; (d) Cyclic stability after 10,000 GCD cycles; (e) Practical application of CuS@$Ti_3C_2T_x$//AC-ASC.

$s^{-1})^{1/2}$ in cyclic voltammetry reflects the charging and discharging behavior, with k_1 determined by Origin software representing the slope of each curve. The product of k_1 and scanning rate (v) yields the current (i). Comparing the capacitive and diffusion pseudo-capacitance of both materials at the same scanning rates, the histogram (Fig. 5g) reveals that CuS@$Ti_3C_2T_x$ exhibits a higher pseudocapacitive contribution than CuS. For instance, at 10 mV s^{-1}, CuS has only 35.2 % capacitive contribution, while CuS@$Ti_3C_2T_x$ shows 65.7 % capacitive contribution. The maximum capacitive contribution from CuS@$Ti_3C_2T_x$ at 50 mV s^{-1} indicates that $Ti_3C_2T_x$ enhances the pseudo-capacitive contribution due to its high conductivity, large superficial area for more active sites, mitigated self-agglomeration of CuS NPs and improved transport of electrons.

DFT simulation is performed using software (VASP Package) to derive the density of state (DOS) and adsorption energy (E_{ad}). The complete structures and electron models of the four rectangular parallelepipeds of Ti_3C_2, $Ti_3C_2T_x$, CuS@Ti_3C_2 and CuS@$Ti_3C_2T_x$ are shown in Fig. 6(a-d), respectively. All samples exhibit negative E_{ad} values, indicating exothermic behavior, with CuS@$Ti_3C_2T_x$ showing the highest adsorption energy of −3.228 eV, suggesting a stable structure and strong adsorption compared to CuS (−2.024 eV) and $Ti_3C_2T_x$ (−2.112 eV) shown in Fig. 6(e). The negative value signifies an exothermic adsorption process, indicating a release of energy upon K^+ion binding to the surface, which enhances ion binding. Stronger interactions are indicated by more negative values, while positive values suggest weaker interactions, with higher positive values indicating even weaker interactions. Fig. 6(f-h) shows the DOS and project density of state (PDOS) of CuS, $Ti_3C_2T_x$ and CuS@$Ti_3C_2T_x$. CuS@$Ti_3C_2T_x$ shows higher E_{ad}, indicating a stronger interaction with adsorbates, compared to CuS, suggesting a high electronic density and strong electronic interactions. The main contribution of the electronic state near the Fermi level is attributed to Ti 2*p*, C 1 s, Cu 2*p* and S 2*p*. In CuS@$Ti_3C_2T_x$, Cu shows the main contribution, while S 2*p*, Ti 2*p* and C 1 s cross the Fermi level. CuS@$Ti_3C_2T_x$ shows higher electron transfer than CuS and $Ti_3C_2T_x$ due to the more active sites, which provide more empty states for CuS NPs, thus mitigating agglomeration and preventing side reactions. Due to the outstanding electrical conductivity of $Ti_3C_2T_x$ and the presence of metallic Cu, there is a high concentration of electrons close to the Fermi level boosting the superior conductivity. These characteristics enhance the electron transfer rate and reaction kinetics.

In the asymmetric supercapacitor (ASC), the CuS@$Ti_3C_2T_x$ electrode serves as the anode, a 7 M KOH aqueous solution is the electrolyte and AC is the cathode, Fig. S11. To optimize the performance of the CuS@$Ti_3C_2T_x$ electrode in the asymmetric supercapacitor, the AC mass loading on the cathode is determined by the charge balance theorem [59]. The CV curves of both electrodes are presented in Fig. 7a, where the CuS@$Ti_3C_2T_x$ electrode exhibits a voltage window of 0–0.6 V, while the AC electrode has a voltage window of −1 to 0 V. These voltage windows result in a compatible match at a scanning rate of 20 mV s^{-1}, thus extending the potential window of CuS@$Ti_3C_2T_x$//AC-ASC to 0–1.6 V. To explore the maximum operating voltage range, CV curves are acquired from CuS@$Ti_3C_2T_x$//AC-ASC in various potential windows, as shown in Fig. 7b. The CV curves display a similar shape until the potential reaches 1.6 V, at 1.7 V significant polarization occurs due to the precipitation of oxygen resulting from the decomposition of water-based electrolytes, as indicated by the red dotted circles [60]. However, the CV curve of the CuS@$Ti_3C_2T_x$//AC-ASC in Fig. 7c maintains a stable shape within the potential window of 0 −1.6 V, indicating excellent electrochemical stability. Furthermore, the area under the CV curve increases gradually with scanning rates, indicating that CuS@$Ti_3C_2T_x$//AC-ASC has excellent properties. Fig. 7d shows the b-values of CuS@$Ti_3C_2T_x$//AC-ASC calculated in different potential windows to determine the pseudocapacitive characteristics. The slope (b-value) is improved as the potential is increased from 1 to 1.6 V, indicating superior pseudocapacitive characteristics. To further investigate the performance of the CuS@$Ti_3C_2T_x$//AC-ASC device, GCD is conducted in the current density range of 1–30 A g^{-1}, as shown in Fig. 7e. The high regularity of the GCD curve indicates a highly reversible charge/discharge process. The specific capacitance of the CuS@$Ti_3C_2T_x$//AC-ASC is calculated from the discharge time and the total mass of the two electrode materials, as shown in Fig. 7f. CuS@$Ti_3C_2T_x$//AC-ASC device exhibits a maximum specific capacitance of 361.14 F g^{-1} at 1 A g^{-1}. Even after 30 folds, the current density remains stable. CuS@$Ti_3C_2T_x$//AC-ASC still shows a specific capacitance of 150.5 F g^{-1} and an excellent rate capability of 41.5 %.

The Nyquist plots of CuS@$Ti_3C_2T_x$//AC-ASC device before and after

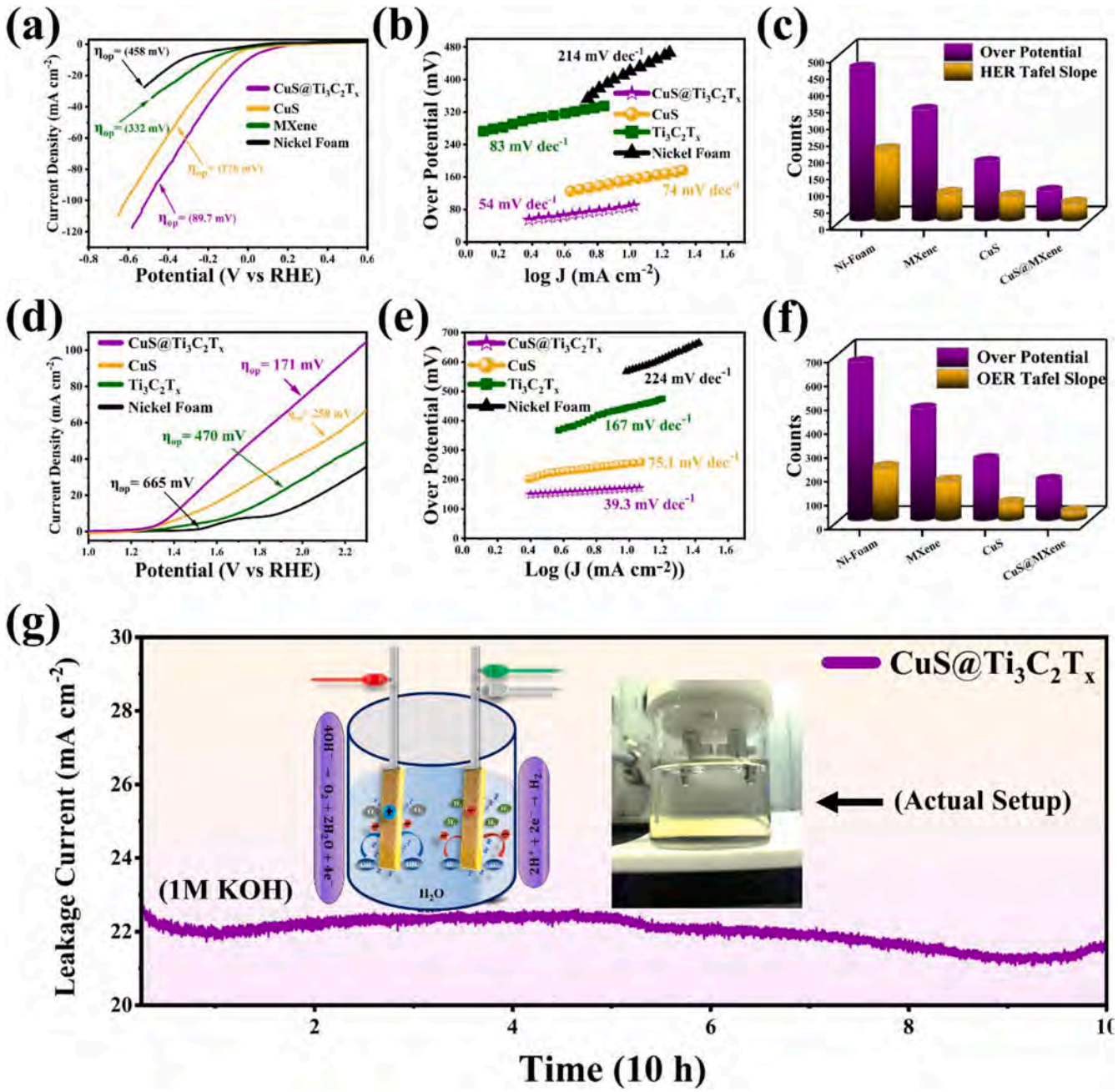

Fig. 9. HER and OER properties of $Ti_3C_2T_x$, CuS, CuS@$Ti_3C_2T_x$, and NF: (a) HER plots, (b) HER Tafel plots, (c) Comparison of overpotential and tafel slope for HER; (d) OER plots; (e) OER Tafel plots; (f) Comparison for OER; (g) Chronoamperometry results with the inset showing the schematic of overall water splitting with experimental setup.

10,000 cycles are compared, revealing that before the stability test, the ASC shows a lower charge transfer resistance (R_{ct} = 0.65). However, after 10,000 cycles, R_{ct}, R_p and R_w increase slightly due to a decrease in the active material caused by charging and discharging, as shown in Table S1. This increase in R_w after cycling is ascribed to the degradation of electrolyte and decay of voltage along with voltametric distortions. The inclusion of $Ti_3C_2T_x$ into the composite introduces surface defects in CuS, thus enhancing electron transfer, improving the conduction of electrons in the valence band and facilitating electron transfer.

The Bode plots are presented in Fig. S12 and the practical application of the CuS@$Ti_3C_2T_x$//AC-ASC setup is illustrated in Fig. 7h. The CuS@$Ti_3C_2T_x$//AC-ASC device achieves a maximum specific energy density of 36.11 Wh kg^{-1} at a power density of about 600 W kg^{-1} and maintains a specific energy density of 15.05 Wh kg^{-1} at a high-power density of 18 kW kg^{-1}. The CuS@$Ti_3C_2T_x$//AC-ASC device exhibits remarkable enhancement in the energy density compared to supercapacitor electrodes based on MXene, as shown in Fig. 8a [57,61–64]. Fig. 8b shows the CV plot at 50 mV s^{-1} for CuS@$Ti_3C_2T_x$//AC-ASC showcasing outstanding pseudocapacitive contribution 84 %. The diffusive and capacitive phenomena are observed at different scanning rates ranging from 10 to 50 mV s^{-1}, as shown in Fig. 8c. Furthermore, the CuS@$Ti_3C_2T_x$//AC-ASC device shows a capacitance retention rate as high as 98.84 % after 10,000 cycles, as shown in Fig. 8d. Fig. 8e shows the practical application of powering green and red LEDs with CuS@-$Ti_3C_2T_x$//AC-ASC. The remarkable electrochemical performance of the CuS@$Ti_3C_2T_x$//AC-ASC device is attributed to the notable capacity of CuS, the exceptional conductivity of $Ti_3C_2T_x$ and the synergistic effect of both materials. These results indicate that this composite material has

exhibited tremendous potential for the advancement of high-performance supercapacitors.

To gain insights into the redox kinetics of water splitting, linear sweep voltammetry (LSV) analysis combined with overpotential, polarization curves, and stability analysis were conducted in an alkaline electrolyte (1 M KOH), focusing on two key processes: the oxygen evolution reaction (OER) and the hydrogen evolution reaction (HER). In the HER analysis (Fig. S13), the LSV polarization curves of CuS@$Ti_3C_2T_x$, CuS, $Ti_3C_2T_x$, and NF were recorded and are illustrated in Fig. 9a The results show that the electrocatalysts NF, $Ti_3C_2T_x$, and CuS exhibit overpotentials of 458, 332, and 176 mV, respectively, while the CuS@$Ti_3C_2T_x$ composite achieves the most favorable overpotential of 89.7 mV to reach the reference current density of 10 mA cm^{-2}. The reduced overpotential of CuS@$Ti_3C_2T_x$ is attributed to the increased interlayer distance resulting from the etching of Al layers. Additionally, the intercalation of CuS between the $Ti_3C_2T_x$ sheets further decreases the overpotential. To analyze the HER performance of the electrocatalysts in terms of polarization curves, the Tafel slopes are plotted in Fig. 9b. CuS@$Ti_3C_2T_x$ displays the minimum Tafel slope of 54 mV dec^{-1}, suggesting that it possesses a Volmer-Heyrovsky mechanism in the HER, with the Volmer step involving sluggish electron-coupled water dissociation as the rate-determining step. Fig. 9c presents a comparative analysis of the overpotentials and Tafel slopes, similar to Fig. 9(a, b). A schematic illustration of a three-electrode system using CuS@$Ti_3C_2T_x$ as an electrocatalyst for OER is displayed in Fig. S14. Fig. 9d Fig. 9d depicts the OER performance of the CuS-based electrocatalysts using a typical three-electrode system. NF and $Ti_3C_2T_x$ require overpotentials of 665 mV and 470 mV, respectively, while CuS and CuS@$Ti_3C_2T_x$ show significantly lower overpotentials of 258 mV and 171 mV, respectively. For further analysis of the OER response, the Tafel slopes are plotted in Fig. 9e. NF exhibits the largest Tafel slope of 224 mV dec^{-1}, while $Ti_3C_2T_x$ shows a slope of 167 mV dec^{-1}. In contrast, CuS and CuS@-$Ti_3C_2T_x$ demonstrate Tafel slopes of 75.1 mV dec^{-1} and 39.3 mV dec^{-1}, respectively. Fig. 9f compares the overpotentials and OER Tafel slopes of the electrocatalysts and Fig. 9g illustrates that CuS@$Ti_3C_2T_x$ composite remains stable for 10 h and can sustain high current densities during water splitting. The inset illustrates the water-splitting setup, demonstrating the formation of O_2 at the anode and H_2 at the cathode in an alkaline electrolyte (1 M KOH) [65]. The first equation, $4OH^- \rightarrow O^2 + 2H_2O + 4e^{-1}$, describes the oxidation of hydroxide ions (OH^-) to produce oxygen gas (O_2), water (H_2O) and electrons at the anode. This reaction is crucial in generating oxygen during the electrolysis of water. The second equation, ($2H^+ + 2e^- \rightarrow H_2$), represents the reduction of protons (H^+) to form hydrogen gas (H_2) at the cathode. Together, these reactions illustrate the conversion of water into oxygen and hydrogen, showcasing the principles of electrochemical energy conversion. The overall water splitting performance of the CuS@$Ti_3C_2T_x$ composite is depicted in Fig. S15, demonstrating that the material exhibits a minimum potential of 1.42 V at a current density of 10 mA cm^{-2}. This observation suggests that the composite is effective in facilitating the water splitting reaction under the specified conditions. The reduced overpotential and Tafel slope are attributed to the synergistic effect of the composite material.

4. Conclusion

The CuS@$Ti_3C_2T_x$ electrode is designed for ASC and water-splitting applications. By incorporating CuS NPs into the layers of $Ti_3C_2T_x$ nanosheets, additional active sites and a large area are created to mitigate agglomeration and control side reactions. The CuS@$Ti_3C_2T_x$ composite has a remarkable specific capacitance of 957.36 F g^{-1} at 1 A g^{-1} and 99.1 % capacity retention for 10,000 cycles. Analysis of the pseudocapacitance properties of supercapacitors reveals a remarkable capacitive value of 90.3 %. DFT simulations are consistent with the experimental data. The CuS@$Ti_3C_2T_x$//AC-ASC shows a specific capacitance of 361.1 F g^{-1}, 98.84 % capacity retention for 10,000 cycles and an energy density of 36.11 W kg^{-1}. These findings highlight the tremendous potential of the CuS@$Ti_3C_2T_x$//AC in energy storage applications. Furthermore, our analysis reveals that the multilayered structure of CuS@$Ti_3C_2T_x$ enhances electron transfer and increases the efficiency of the OER and HER. LSV provides insights into the redox kinetics, disclosing the smallest Tafel slopes for OER (39.3 mV dec^{-1}) and HER (54 mV dec^{-1}). With its exceptional electrochemical properties, CuS@$Ti_3C_2T_x$ exhibits immense potential as an electrode material for advanced supercapacitors (SCs) and water-splitting applications

CRediT authorship contribution statement

Ayesha Irfan: Writing – original draft, Methodology, Investigation, Formal analysis, Data curation, Conceptualization. **Inaam Ullah:** Methodology, Data curation, Conceptualization. **Mai Li:** Writing – review & editing, Visualization, Validation, Supervision, Resources, Funding acquisition, Data curation, Conceptualization. **Wendong Xu:** Investigation. **Zibo Dong:** Investigation. **Hanxue Zhao:** Investigation. **Haotian Hu:** Investigation. **Nimra Irshad:** Investigation. **Kaishuai Yang:** Software. **Ping Zhong:** Supervision, Resources. **Paul K. Chu:** Resources.

Declaration of competing interest

The authors declare that they have no known competing financial interests or personal relationships that could have appeared to influence the work reported in this paper.

Acknowledgments

The research was funded by the Fundamental Research Funds for the Central Universities (No. 2232024D-31), National Natural Science Foundation of China (No. 22005046), Natural Science Foundation of Shanghai (21ZR1402900) and City University of Hong Kong Donation Research Grants (DON-RMG 9229021 and 9220061).

Supplementary materials

Supplementary material associated with this article can be found, in the online version, at doi:10.1016/j.surfin.2024.105536.

Data availability

Data will be made available on request.

References

[1] S.W. Zhang, B.S. Yin, X.X. Liu, D. Gu, H. Gong, Z. Wang, A high energy density aqueous hybrid supercapacitor with widened potential window through multi approaches, Nano Energy 59 (2019) 41–49, https://doi.org/10.1016/j.nanoen.2019.02.001.

[2] X.X. Li, X.T. Wang, K. Xiao, T. Ouyang, N. Li, Z.Q. Liu, *In situ* formation of consubstantial NiCo2S4 nanorod arrays toward self-standing electrode for high activity supercapacitors and overall water splitting, J. Power Sources 402 (2018) 116–123, https://doi.org/10.1016/j.jpowsour.2018.09.021.

[3] J. Balamurugan, T.T. Nguyen, V. Aravindan, N.H. Kim, S.H. Lee, J.H. Lee, All ternary metal selenide nanostructures for high energy flexible charge storage devices, Nano Energy 65 (2019) 103999, https://doi.org/10.1016/j.nanoen.2019.103999.

[4] D.K. Km, K. Ho Kim, G. Saeed, T. Toupance, Y.K. Jeong, D. Lee, Synthesis and properties of a ternary transition metal compound as positive electrode for high-performance supercapacitors, J. Energy Storage 78 (2024) 110032, https://doi.org/10.1016/j.est.2023.110032.

[5] Y. He, F. Hu, D. Liu, X. He, Q. Li, Y. Sui, J. Qi, Y. Wang, Cattail spike-like Co(OH)F@Co3O4 nanoarrays for high-performance supercapacitors, J. Energy Storage 58 (2023) 106377, https://doi.org/10.1016/j.est.2022.106377.

[6] W. Xu, M. Li, W. Hasan, Z. Meng, H. Hu, I. Ullah, A. Irfan, J. Shen, P.K. Chu, Composition-optimized NiGa-LDH on MOF-derived and cobalt-nanoparticles-embedded carbon flakes for enhanced potassium-ion storage, Chem. Eng. J. (2024) 155931, https://doi.org/10.1016/j.cej.2024.155931.

[7] X. Zhang, J. Wang, Y. Sui, F. Wei, J. Qi, Q. Meng, Y. He, D. Zhuang, Hierarchical nickel–cobalt phosphide/phosphate/carbon nanosheets for high-performance

supercapacitors, ACS Appl. Nano Mater. 3 (2020) 11945–11954, https://doi.org/10.1021/acsanm.0c02507.
[8] H. Zhao, M. Li, J. Du, Y. Lei, A. Irfan, M. Imran, C. Wang, J. He, Z. Sun, P.K. Chu, CdSe-nanoparticles-regulated synthesis of ZnCo-MOFs derived conductive porous carbon nanoflakes on carbon cloth for flexible sodium-ion supercapacitors, Electrochim. Acta 471 (2023) 143366, https://doi.org/10.1016/j.electacta.2023.143366.
[9] S.L. Didi Liu, Y. He, C. Liu, Q. Li, Y. Sui, J. Qi, P. Zhang, C. Chen, Z. Chen, S. Liu, Co (OH) F@ CoP/CC core-shell nanoarrays for high-performance supercapacitors, J. Energy Storage 55 (2022) 105417, https://doi.org/10.1016/j.est.2022.105417.
[10] Y. He, D. Liu, H. Zhao, J. Wang, Y. Sui, J. Qi, Z. Chen, P. Zhang, C. Chen, D. Zhuang, Carbon-coated NiMn layered double hydroxides/Ni3S2 nanocomposite for high performance supercapacitors, J. Energy Storage 41 (2021) 103003, https://doi.org/10.1016/j.est.2021.103003.
[11] W. Fu, W. Han, H. Zha, J. Mei, Y. Li, Z. Zhang, Erqing Xie, Nanostructured CuS networks composed of interconnected nanoparticles for asymmetric supercapacitors, Phys. Chem. Chem. Phys. 18 (2016) 24471–24476, https://doi.org/10.1039/C6CP02228F.
[12] X.Z. Muhammad Sufyan Javed, S. Ali, A. Mateen, M. Idrees, M. Sajjad, S. Batool, A. Ahmad, M. Imran, T. Najam, W. Han, Heterostructured bimetallic–sulfide@ layered Ti3C2Tx–MXene as a synergistic electrode to realize high-energy-density aqueous hybrid-supercapacitor, Nano Energy 101 (2022) 107624, https://doi.org/10.1016/j.nanoen.2022.107624.
[13] H. Heydari, S. Ebrahim Moosavifard, M. Shahraki, S. Elyasi, Facile synthesis of nanoporous CuS nanospheres for high-performance supercapacitor electrodes, J. Energy Chem. 26 (2017) 726–767, https://doi.org/10.1016/j.jechem.2017.03.007.
[14] M.T. Ilyas, A. Fazal, Z. Ur Rehman, M. Ali Raza, BS. Almutairi, M.J Iqbal, S. Ali, Substantial performance of copper sulfide nanotubes at high current densities for energy storage applications, J. Energy Storage 85 (2024) 111055, https://doi.org/10.1016/j.est.2024.111055.
[15] X.Z. Jinxue Guo, Y. Sun, X. Zhang, L. Tang, X. Zhang, Double-shell CuS nanocages as advanced supercapacitor electrode materials, J. Power Sources 355 (2017) 31–35, https://doi.org/10.1016/j.jpowsour.2017.04.052.
[16] S.Z. Zongrong Ying, J. Yue, T. Ju, Y. Zhang, J. Xie, Q. Wang, 3D hierarchical CuS microflowers constructed on copper powders-filled nickel foam as advanced binder-free electrodes, J. Alloys. Compd. 821 (2020) 153437, https://doi.org/10.1016/j.jallcom.2019.153437.
[17] S. Zhai, K. Jin, M. Zhou, Z. Fan, H. Zhao, Y. Zhao, X. Li, Z. Cai, *In-situ* growth of flower-like CuS microsphere on carbonized cotton for high-performance flexible supercapacitor, Colloids Surf. A Physicochem. Eng. Asp. 575 (2019) 75–83, https://doi.org/10.1016/j.colsurfa.2019.05.010.
[18] Y. Liu, Z. Zhou, S. Zhang, W. Luo, G. Zhang, Controllable synthesis of CuS hollow microflowers hierarchical structures for asymmetric supercapacitors, Appl. Surf. Sci. 442 (2018) 711–719, https://doi.org/10.1016/j.apsusc.2018.02.220.
[19] S.I. El-Hout, S.G. Mohamed, A. Gaber, S.Y. Attia, A. Shawky, S.M. El-Sheikh, High electrochemical performance of rGO anchored CuS nanospheres for supercapacitor applications, J. Energy Storage 34 (2021) 102001, https://doi.org/10.1016/j.est.2020.102001.
[20] L.L. Juguo Dai, Z. Tang, Y. Lv, H. Xie, H. Zuo, C. Yang, X. Wang, M. Fan, Y. Xu, L. Dai, Strategy for constructing highly stable supercapacitors: channeling of thin-layer polyaniline to enhance pseudo-capacitance of the CuS/polyaniline@ MoS2 composites, Compos. Sci. Technol. 219 (2022) 109240, https://doi.org/10.1016/j.compscitech.2021.109240.
[21] Y.A. Dakka, J. Balamurugan, R. Balaji, N.H. Kim, J.H. Lee, Advanced Cu0. 5Co0. 5Se2 nanosheets and MXene electrodes for high-performance asymmetric supercapacitors, Chem. Eng. J. 385 (2020) 123455, https://doi.org/10.1016/j.cej.2019.123455.
[22] S. De, S. Acharya, S. Sahoo, J.J. Shim, Ganesh Chandra Nayak, From 0D to 3D MXenes: their diverse syntheses, morphologies and applications, Mater. Chem. Front. 6 (2022) 818–842, https://doi.org/10.1039/D2QM00002D.
[23] S. De, S. Acharya, C. Kumar Maity, S. Sahoo, MXene (Ti3C2Tx)-/amine-functionalized graphene-supported self-assembled Co9S8 nanoflower for Ultrastable hybrid supercapacitor, Ind. Eng. Chem. Res. 61 (2022) 7727–7738, https://doi.org/10.1021/acs.iecr.2c00810.
[24] Y. Han, Z. Liu, C. Wang, Li Guo, Y. Wang, Construction of rod-like cobalt-pyridinedicarboxylic acid/MXene nanosheets composites for hydrogen evolution reaction and supercapacitor, J. Colloid Interface Sci. 661 (2024) 139–149, https://doi.org/10.1016/j.jcis.2024.01.152.
[25] J. Xiao, P. Yu, K. Zhao, H. Gao, Two-dimensional transition metal carbide (Ti0. 5V0. 5) 3C2Tx MXene as high performance electrode for flexible supercapacitor, J. Colloid Interface Sci. 639 (2023) 233–240, https://doi.org/10.1016/j.jcis.2023.02.068.
[26] Y. Xie, H. Zhang, H. Huang, Z. Wang, Z. Xu, H. Zhao, Y. Wang, N. Chen, W. Yang, High-voltage asymmetric MXene-based on-chip micro-supercapacitors, Nano Energy 74 (2020) 104928, https://doi.org/10.1016/j.nanoen.2020.104928.
[27] Y.Z. Ningjun Chen, S. Zhang, H. Huang, C. Zhang, X. Zheng, X. Chu, H. Zhang, W. Yang, J. Chen, Tailoring Ti_3CNT_x MXene via an acid molecular scissor, Nano Energy 85 (2021) 106007, https://doi.org/10.1016/j.nanoen.2021.106007.
[28] J.H. Haichao Huang, Z. Wang, H. Zhang, L. Jin, N. Chen, Y. Xie, X. Chu, B. Gu, W. Deng, Scalable, and low-cost treating-cutting-coating manufacture platform for MXene-based on-chip micro-supercapacitors, Nano Energy 69 (2020) 104431, https://doi.org/10.1016/j.nanoen.2019.104431.
[29] Z. Li, M. Jiang, F. Wu, L. Wu, X. Zhang, L. Li, Synergistic *in-situ* intercalation and surface modification strategy for Ti3C2Tx MXene-based supercapacitors with enhanced electrochemical energy storage, J. Energy Storage 84 (2024) 110772, https://doi.org/10.1016/j.est.2024.110772.
[30] A. VahidMohammadi, J. Rosen, Y. Gogotsi, The world of two-dimensional carbides and nitrides (MXenes), Science 372 (2021) 6547, https://doi.org/10.1126/science.abf1581 (1979).
[31] Y. Li, H. Shao, Z. Lin, J. Lu, L. Liu, B. Duployer, P.O.Å. Persson, P. Eklund, L. Hultman, M. Li, K. Chen, X.H. Zha, S. Du, P. Rozier, Z. Chai, E. Raymundo-Piñero, P.L. Taberna, P. Simon, Q. Huang, A general Lewis acidic etching route for preparing MXenes with enhanced electrochemical performance in non-aqueous electrolyte, Nat. Mater. 19 (2020) 894–899, https://doi.org/10.1038/s41563-020-0657-0.
[32] M.W.H. Ebrima Ceesay, E. Mazhar, S.U. Awan, S. Rizwan, Improved pseudocapacitor and water splitting in cobalt-anchored vanadium carbide MXene nanocomposite, Int. J. Hydrog. Energy 56 (2024) 140–146, https://doi.org/10.1016/j.ijhydene.2023.12.066.
[33] M. Seredych, C.E. Shuck, D. Pinto, M. Alhabeb, E. Precetti, G. Deysher, B. Anasori, N. Kurra, Y. Gogotsi, High-temperature behavior and surface chemistry of carbide MXenes studied by thermal analysis, Chem. Mater. 31 (2019) 3324–3332, https://doi.org/10.1021/acs.chemmater.9b00397.
[34] J. Fu, L. Li, J.M. Yun, D. Lee, B.K. Ryu, K.H. Kim, Two-dimensional titanium carbide (MXene)-wrapped sisal-Like NiCo2S4 as positive electrode for High-performance hybrid pouch-type asymmetric supercapacitor, Chem. Eng. J. 375 (2019), https://doi.org/10.1016/J.CEJ.2019.121939.
[35] T. Zhang, R. Wang, J. Xiao, L. Li, X. Ma, W. Zhang, CoS nanowires grown on Ti3C2Tx are promising electrodes for supercapacitors: high capacitance and remarkable cycle capability, J. Colloid Interface Sci. 602 (2021) 123–130, https://doi.org/10.1016/j.jcis.2021.06.011.
[36] Z. Lin, K. Li, Y. Tong, W. Wu, X. Cheng, H. Wang, P. Chen, P. Diao, Engineering coupled NiSx-WO2. 9 Heterostructure as pH-universal electrocatalyst for hydrogen evolution reaction, ChemSusChem 16 (2023) e202201985, https://doi.org/10.1002/cssc.202201985.
[37] X. Ren, Y. Tong, The self-reconstruction of Co-modified bimetallic hydroxysulfide nanosheet arrays for efficient hydrazine assisted water splitting, Int. J. Hydrog. Energy 49 (2024) 489–497, https://doi.org/10.1016/j.ijhydene.2023.08.109.
[38] X. Liu, J. Zhang, J. Xu, Y. Li, Y. Du, Y. Jiang, K. Lin, Hydroxyl-modified Nb4C3Tx MXene@ ZnIn2S4 sandwich structure for photocatalytic overall water splitting, J. Colloid Interface Sci. 633 (2023) 992–1001, https://doi.org/10.1016/j.jcis.2022.11.142.
[39] K. Li, Y. Tong, J.F. He, X.Y. Liu, P. Chen, Anion-modulated CoP electrode as bifunctional electrocatalyst for anion-exchange membrane hydrazine-assisted water electrolyser, Mater. Horiz. 10 (2023) 5277–5287, https://doi.org/10.1039/D3MH00872J.
[40] K. Huang, C. Lv, C. Li, H. Bai, X. Meng, Ti_3C_2 MXene supporting platinum nanoparticles as rapid electrons transfer channel and active sites for boosted photocatalytic water splitting over g-C3N4, J. Colloid Interface Sci. 636 (2023) 21–32, https://doi.org/10.1016/j.jcis.2022.12.169.
[41] J. Wang, X. Yue, Y. Yang, S. Sirisomboonchai, P. Wang, X. Ma, A. Abudula, G. Guan, Earth-abundant transition-metal-based bifunctional catalysts for overall electrochemical water splitting: a review, J. Alloys. Compd. 819 (2020), https://doi.org/10.1016/j.jallcom.2019.153346.
[42] K. Dashtian, S. Shahsavarifar, M. Usman, Y. Joseph, M.R. Ganjali, Z. Yin, M. Rahimi-Nasrabadi, A comprehensive review on advances in polyoxometalate based materials for electrochemical water splitting, Coord. Chem. Rev. 504 (2024) 215644, https://doi.org/10.1016/j.ccr.2023.215644.
[43] L. Zhang, Y. Lei, W. Xu, D. Wang, Y. Zhao, W. Chen, Xu Xiang, X. Pang, B. Zhang, H. Shang, Highly active and durable nitrogen-doped CoP/CeO2 nanowire heterostructures for overall water splitting, Chem. Eng. J. 460 (2023) 141119, https://doi.org/10.1016/j.cej.2022.141119.
[44] Y. Lei, L. Zhang, W. Xu, C. Xiong, W. Chen, X. Xiang, B. Zhang, H. Shang, Carbon-supported high-entropy Co-Zn-Cd-Cu-Mn sulfide nanoarrays promise high-performance overall water splitting, Nano Res. 15 (2022) 6054–6061, https://doi.org/10.1007/s12274-022-4304-8.
[45] Y. Lei, L. Zhang, D. Zhou, C. Xiong, Y. Zhao, W. Chen, X. Xiang, H. Shang, B. Zhang, Construction of interconnected NiO/CoFe alloy nanosheets for overall water splitting, Renew. Energy 194 (2022) 459–468, https://doi.org/10.1016/j.renene.2022.05.124.
[46] X. Wang, N. Zhang, S. Guo, H. Shang, X. Luo, Z. Sun, Z. Wei, Y. Lei, L. Zhang, D. Wang, Y. Zhao, F. Zhang, L. Zhang, X. Xiang, W. Chen, B. Zhang, pd Orbital hybridization induced by asymmetrical FeSn dual atom sites promotes the oxygen reduction reaction, J. Am. Chem. Soc. 146 (2024) 21357–21366, https://doi.org/10.1021/jacs.4c03576.
[47] H. Li, Y. Wen, X. Zhu, J. Wang, L. Zhang, B. Sun, Novel heterostructure of a MXene@NiFe-LDH nanohybrid with superior peroxidase-like activity for sensitive colorimetric detection of glutathione, ACS Sustain. Chem. Eng. 8 (2019) 520–526, https://doi.org/10.1021/acssuschemeng.9b05987.
[48] D. Xu, Z. Kang, H. Zhao, Y. Ji, W. Yao, D. Ye, J. Zhang, Coupling heterostructured CoP-NiCoP nanopin arrays with MXene (Ti3C2Tx) as an efficient bifunctional electrocatalyst for overall water splitting, J. Colloid Interface Sci. 639 (2023) 223–232, https://doi.org/10.1016/j.jcis.2023.02.052.
[49] S.K. Godlaveeti, S.K. Arla, A. El-marghany, A.R. Somala, V.K.N. Boya, R. R. Nagireddy, S.W. Joo, Nanostructured 3-D nano-bricks shaped CuO–0-D particle shaped Co3O4 composite for superior photo-electrochemical water splitting, Int. J. Hydrog. Energy 58 (2024) 1000–1008, https://doi.org/10.1016/j.ijhydene.2024.01.177.

[50] C.E. Shuck, A. Sarycheva, M. Anayee, A. Levitt, Y. Zhu, S. Uzun, V. Balitskiy, V. Zahorodna, O. Gogotsi, Y. Gogotsi, Scalable synthesis of Ti3C2Tx mxene, Adv. Eng. Mater. 22 (2020) 1901241, https://doi.org/10.1002/adem.201901241.
[51] M. Ghidiu, J. Halim, S. Kota, D. Bish, Y. Gogotsi, M.W. Barsoum, Ion-exchange and cation solvation reactions in Ti3C2 MXene, Chem. Mater. 28 (2016) 3507–3514, https://doi.org/10.1021/acs.chemmater.6b01275.
[52] H. Liang, W. Shuang, Y. Zhang, S. Chao, H. Han, X. Wang, H. Zhang, L. Yang, Graphene-like multilayered CuS nanosheets assembled into flower-like microspheres and their electrocatalytic oxygen evolution properties, ChemElectroChem 5 (2018) 494–500, https://doi.org/10.1002/celc.201701074.
[53] K.V.G. Raghavendra, C.V.V.M. Gopi, R. Vinodh, I.K. Durga, H. Kim, One-step facile synthesis of dense cloud-like tiny bundled nanoparticles of CuS nanostructures as an efficient electrode material for high-performance supercapacitors, J. Energy Storage 27 (2020) 101148, https://doi.org/10.1016/j.est.2019.101148.
[54] N. Li, Y. Zhang, M. Jia, X. Lv, X. Li, R. Li, X. Ding, Y.Z. Zheng, X. Tao, 1T/2H MoSe2-on-MXene heterostructure as bifunctional electrocatalyst for efficient overall water splitting, Electrochim. Acta 326 (2019), https://doi.org/10.1016/j.electacta.2019.134976.
[55] J. Zhang, H. Feng, J. Yang, Q. Qin, H. Fan, C. Wei, W. Zheng, Solvothermal synthesis of three-dimensional hierarchical CuS microspheres from a Cu-based ionic liquid precursor for high-performance asymmetric supercapacitors, ACS Appl. Mater. Interfaces 7 (2015) 21735–21744, https://doi.org/10.1021/acsami.5b04452.
[56] D. Zhang, J. Cao, X. Zhang, N. Insin, R. Liu, J. Qin, NiMn layered double hydroxide nanosheets in-situ anchored on Ti3C2 MXene via chemical bonds for superior supercapacitors, ACS Appl. Energy Mater. 3 (2020) 5949–5964, https://doi.org/10.1021/acsaem.0c00863.
[57] Z. Pan, Fa Cao, X. Hu, X. Ji, A facile method for synthesizing CuS decorated Ti3C2 MXene with enhanced performance for asymmetric supercapacitors, J. Mater. Chem. A 7 (2019) 8984–8992, https://doi.org/10.1039/C9TA00085B.
[58] J. Yang, C. Wang, H. Ju, Y. Sun, S. Xing, J. Zhu, Q. Yang, Integrated quasiplane heteronanostructures of MoSe2/Bi2Se3 hexagonal nanosheets: synergetic electrocatalytic water splitting and enhanced supercapacitor performance, Adv. Funct. Mater. 27 (2017) 1703864, https://doi.org/10.1002/adfm.201703864.
[59] J. Zhang, X. Lu, J. Zhang, H. Li, B. Huang, B. Chen, J. Zhou, S. Jing, Metal-ions intercalation mechanism in layered anode from first-principles calculation, Front. Chem. 9 (2021), https://doi.org/10.3389/fchem.2021.677620.
[60] J. Fu, L. Li, J. Yun, D. Lee, B. Ryu, K. Kim, Two-dimensional titanium carbide (MXene)-wrapped sisal-Like NiCo2S4 as positive electrode for High-performance hybrid pouch-type asymmetric supercapacitor, Chem. Eng. J. 375 (2019) 121939, https://doi.org/10.1016/j.cej.2019.121939.
[61] Y. Liu, J. Gong, J. Wang, C. Hu, M. Xie, X. Jin, S. Wang, Y. Dai, Facile fabrication of MXene supported nickel-cobalt selenide ternary composite via one-step hydrothermal for high-performance asymmetric supercapacitors, J. Alloys. Compd. 899 (2022) 163354, https://doi.org/10.1016/j.jallcom.2021.163354.
[62] Y. Luo, Y. Tian, Y. Tang, X. Yin, Wenxiu Que, 2D hierarchical nickel cobalt sulfides coupled with ultrathin titanium carbide (MXene) nanosheets for hybrid supercapacitors, J. Power Sources 482 (2021) 228961, https://doi.org/10.1016/j.jpowsour.2020.228961.
[63] S. Venkateshalu, Ti3C2Tx MXene and Vanadium nitride/Porous carbon as electrodes for asymmetric supercapacitors, Electrochim. Acta 341 (2020) 136035, https://doi.org/10.1016/j.electacta.2020.136035.
[64] J. Fu, J. Yun, S. Wu, L. Li, L. Yu, K. Kim, Architecturally robust graphene-encapsulated MXene Ti2CTx@Polyaniline composite for high-performance pouch-type asymmetric supercapacitor, ACS Appl. Mater. Interfaces 10 (2018) 34212–34221, https://doi.org/10.1021/acsami.8b10195.
[65] Q.S. Tong, P. Chen, L. Chen, Z. Fei, P.J. Dyson, Nitrogen-incorporated cobalt sulfide/Graphene hybrid catalysts for overall water splitting, ChemSusChem 13 (2020) 5112, https://doi.org/10.1002/cssc.202001413.

Supporting Information

Synergistic Effects of Hybrid CuS@$Ti_3C_2T_x$/MXene for Enhanced Super capacitive Energy Storage and Efficient Water Splitting

Ayesha Irfan[a], Inaam Ullah[a], Mai Li[a*], Wendong Xu[a], Zibo Dong[a], Hanxue Zhao[a], Haotian Hu [a], Nimra Irshad[a], Kaishuai Yang[b], Ping Zhong[a*], Paul K. Chu[c]

[a] College of Science, Donghua University, Shanghai 201620, China

[b] School of Electronic and Information Engineering, Changshu Institute of Technology, Suzhou 215000, P. R. China

[c] Department of Physics, Department of Materials Science and Engineering, and Department of Biomedical Engineering, City University of Hong Kong, Tat Chee Avenue, Kowloon, Hong Kong, China

* Corresponding authors: E-mail: limai@dhu.edu.cn (M. Li); pzhong937@dhu.edu.cn (Z. Ping)

Contents

S1. Preparation of Electrodes:

The CuS, $Ti_3C_2T_x$, and CuS@$Ti_3C_2T_x$ composites were synthesized through hydrothermal and solvothermal techniques. These composites were then deposited onto pre-treated nickel foam (NF) to create the working electrodes. To ensure the removal of excessive oxides, the NF was conditioned in 3 M HCl for 3 hours, followed by 6 hours of vacuum drying at 60°C.

A synthesis material ink (SMI) was prepared by combining 500 µl of DI water, 50 µl of nafion, 450 µl of isopropyl alcohol, and 10 mg of the active material (CuS, $Ti_3C_2T_x$, or CuS@$Ti_3C_2T_x$) in a glass vial. The mixture was sonicated in an ice bath for 1 hour and then uniformly coated on the treated NF. The coated NF was dried at 80°C for 5 hours.

In the three-electrode setup, the reference electrode was Ag/AgCl with a potential of 0.197 V, the counter electrode was a graphite plate, and the working electrode was either CuS, $Ti_3C_2T_x$, or CuS@$Ti_3C_2T_x$. For the energy storage calculations, the electrolyte consisted of 1.0 M KOH, supplemented with 0.2 mM potassium hexacyanoferrate (II) ($K_4[Fe(CN)_6]$), while for water splitting, only 1 M KOH was used. The CHI660E electrochemical workstation was utilized for various tests including cyclic voltammetry (CV), galvanostatic charging-discharging (GCD), electrochemical impedance spectroscopy (EIS) in the frequency range of 0.1 Hz to 1 MHz, linear sweep voltammetry (LSV), and chronoamperometry test (for 10 hours).

In the asymmetric supercapacitor (ASC) configuration, the CuS@$Ti_3C_2T_x$ electrode served as the positive electrode, while Active Carbon was used as the counter electrode. Active Carbon was synthesized by mixing 10% carbon black (CB) and 80% active carbon in a solution containing 10% polytetrafluoroethylene (PTFE) and ethanol. The mixture was stirred at a slow speed for 48 hours. The resulting mixture was evenly applied onto the NF substrate and dried under vacuum at 60°C for 24 hours. The total mass of the electrode materials ranged from 2.5

to 3.5 mg cm^{-2}. The ASC was assembled by separating the positive and negative electrodes with an organic separator, and the electrolyte used was 7 M KOH.

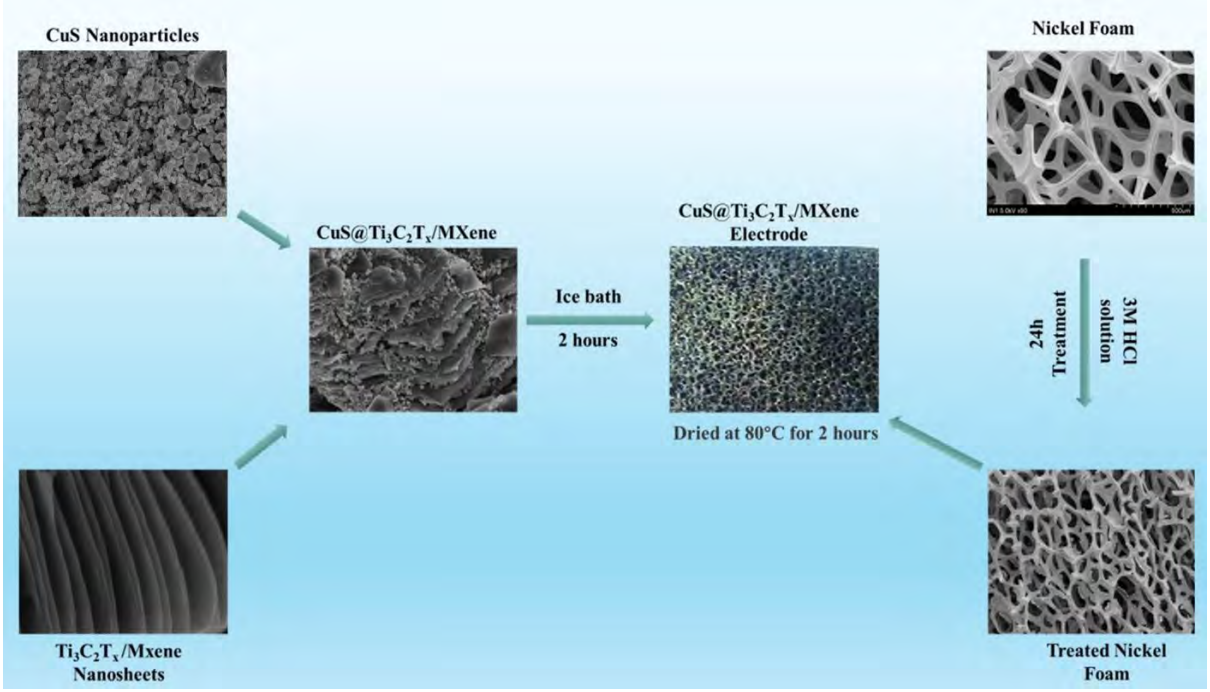

Figure S 1. Electrode formation process illustrated by SEM images.

S2. Materials characterization:

The morphology and crystal structure of the electrocatalyst were observed and studied by using Scanning Electron Microscopy (SEM) on the S4800 (HITACHI, Tokyo, Japan) and X-ray Diffraction (XRD) on the D/max-2550VB+/PC (Rigaku, Tokyo, Japan). The chemical states and elemental composition of the synthesized electrocatalyst were examined and analyzed by X-ray Photoelectron Spectroscopy (XPS) on ESCALB 250XI (Thermo Fisher, Waltham, MA USA), X-Ray Diffraction Spectrometry (EDS) & Transmission Electron Microscopy (TEM)

on the JEM 2100 F (JEOL, Tokyo Japan) at 200kV, Selected-Area Electron Diffraction (SAED) on the X-MAX 80TLE (Oxford Instrument, Oxford, England).

S2.1 Density-functional theory calculations

The density-functional theory (DFT) calculations were carried out using the Vienna ab initio simulation package (VASP) [1],[2]. For the treatment of pseudopotentials and exchange correlation functionals, the project-augmented-wave (PAW) [3] method and the Perdew-Burke-Ernzerhof (PBE) generalized gradient approximation (GGA) [4] method was employed. To ensure accurate results, a plane wave cutoff of 520 eV was set for the kinetic energy, and all self-consistent field computations were performed with a convergence criterion of 1×10^{-5} eV. In order to determine the adsorption energies of sodium ions on MXene, CuS, and CuS@$Ti_3C_2T_x$, three computational models in the form of rectangular parallelepipeds were constructed. These models had dimensions of 8.5 Å × 4.9 Å × 25 Å and consisted of MXene, CuS, and CuS composite with $Ti_3C_2T_x$, respectively. The CuS layer had a thickness of 5.3 Å. To eliminate any interactions between adjacent periodic images, each model was separated by a 15 Å vacuum layer along the z-axis. The Monkhorst-Pack [5] k-mesh of 4 × 7 × 1 was utilized for the Brillouin zone integration.

S2.2 Electrochemical measurements:

The electrochemical evaluation was conducted using the CHI660E electrochemical workstation. The working electrodes consisted of NF, CuS, $Ti_3C_2T_x$, CuS@$Ti_3C_2T_x$ with 1.0 M KOH serving as the electrolyte. The reference electrode used was a Silver/Silver Chloride (Ag/AgCl), and the counter electrode was a graphite plate (10×10×3 mm). The mass loading was set at 2.86 mg cm^{-2}. In the three-electrode system, the potential was applied between the reference and working electrodes, while the current was measured across the counter and

working electrodes. To determine the electrochemical properties, cyclic voltammetry (CV), galvanostatic charging-discharging (GCD), and electrochemical impedance spectroscopy (EIS) were performed. The potential window of the electrodes was determined to be 0V-0.6V. The mass specific capacitance (C_m, F g^{-1}) and area capacitance (C_a, F cm^{-2}) were assessed by constant current charging and discharging (GCD) according to:

$$C_m = \frac{It}{m\Delta V} \text{ ---------- (S2)}$$

$$C_a = \frac{It}{S\Delta V} \text{ ---------- (S3)}$$

where ΔV is the discharging voltage window, t is the discharging duration (s), I indicate discharging current (A), m is the mass of the active materials (g), and S is the surface area (cm^2).

The energy density (E, Wh kg^{-1}) and power density (P, W kg^{-1}) were calculated by:

$$E = \frac{C_m V^2}{2} \times \frac{1000}{3600} \text{ ---------- (S4)}$$

$$P = \frac{3600E}{\Delta t} \text{ ---------- (S5)}$$

where Δt denotes the discharge time(s) and V is the voltage window(V).

The potential vs Reduced Hydrogen Electrode (RHE) was calculated using Nernst Equation,

$$V_{RHE} = 0.197 + 0.059 \times pH + V_{Ag/AgCl/KCl} \text{ ------- (S6)}$$

Where potential vs. RHE is represented by V_{RHE}, 0.197 V is standard potential of Ag/AgCl electrode at 25°C, 0.059 is Nernst Constant and pH is the pH value of the electrolyte (pH~13.9) used for testing.

S3. SEM, TEM and HRTEM images:

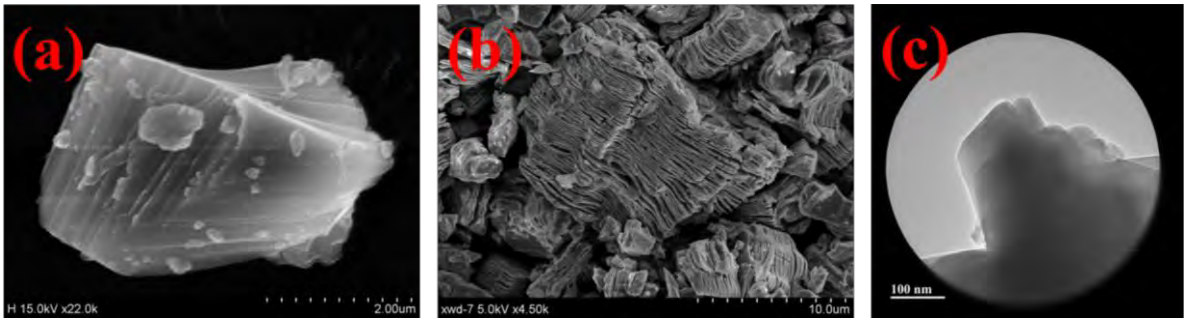

Figure S 2. SEM images of (a) Ti_3AlC_2 (b) $Ti_3C_2T_x$; HRTEM image of (c) $Ti_3C_2T_x$.

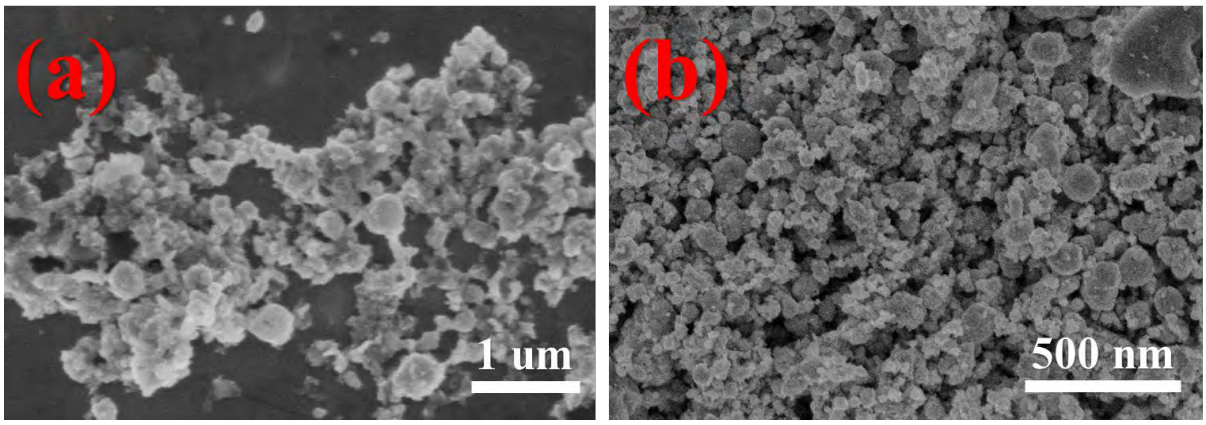

Figure S 3. (a, b) SEM images of CuS.

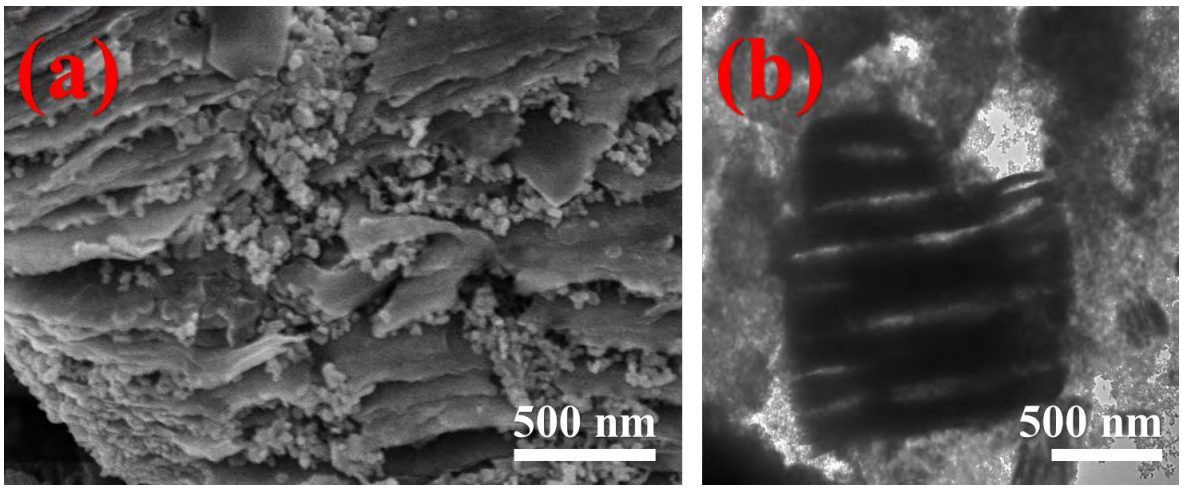

Figure S 4. Images of CuS@$Ti_3C_2T_x$/MXene, (a) SEM (b) TEM.

S4. Electrochemical Characterizations:

To ensure the reliability and reproducibility of our results, each experiment for the prepared electrodes (CuS@$Ti_3C_2T_x$, CuS, and $Ti_3C_2T_x$) was conducted five times. The experiment that exhibited the closest alignment with the calculated mean values and the minimum deviation was selected for further analysis.

To verify the accuracy and consistency of our findings, we assessed the electrochemical properties of each electrode sample. Figure S5 displays the cyclic voltammetry (CV) curves along with the corresponding error bars and standard deviations for the anodic and cathodic peaks of all electrodes.

In Figure S5(a), the CV curves for five replicates of CuS@$Ti_3C_2T_x$ are presented, showcasing minimal variations across all measurements. The associated error bars for the anodic and cathodic peaks are illustrated in Figures S5(d) and (g), with the mean values indicated by a magenta line. Notably, the results for the third electrode align closely with the mean, while the other electrodes exhibit some deviations. Similarly, Figure S5(b) illustrates the CV curves for five replicates of CuS, again revealing small variations. The error bars for the anodic and cathodic peaks are depicted in Figure S5(e) and (h), respectively. In this case, the first electrode closely aligns with the mean value, whereas the remaining electrodes show noticeable deviations. Figure S5(c) presents the CV curves for five replicates of $Ti_3C_2T_x$, showcasing minimal variation. The error bars for the anodic and cathodic peaks are shown in Figures S5(f) and (i), with the mean values also indicated by a magenta line. Here, the second electrode closely matches the mean, while the others demonstrate some degree of variation.

The standard deviations for the anodic peak currents are summarized in Figure S5 (j). For CuS@$Ti_3C_2T_x$, the anodic peak has a standard deviation of 0.6485, resulting in a relative standard deviation of 0.5387%. The CuS electrodes show a standard deviation of 0.4388,

corresponding to a relative standard deviation of 0.5849%. For $Ti_3C_2T_x$, the anodic peak has a standard deviation of 1.0909, with a relative standard deviation of 2.390%. In Figure S5(k), we present the standard deviations for the cathodic peak currents. The cathodic peak values for CuS@$Ti_3C_2T_x$ show a standard deviation of 0.5427 and a relative standard deviation of 0.5387%. The CuS electrodes display a standard deviation of 0.2724, with a relative standard deviation of 0.5849%. Lastly, the $Ti_3C_2T_x$ electrodes show a standard deviation of 0.5980, resulting in a relative standard deviation of 2.390%.

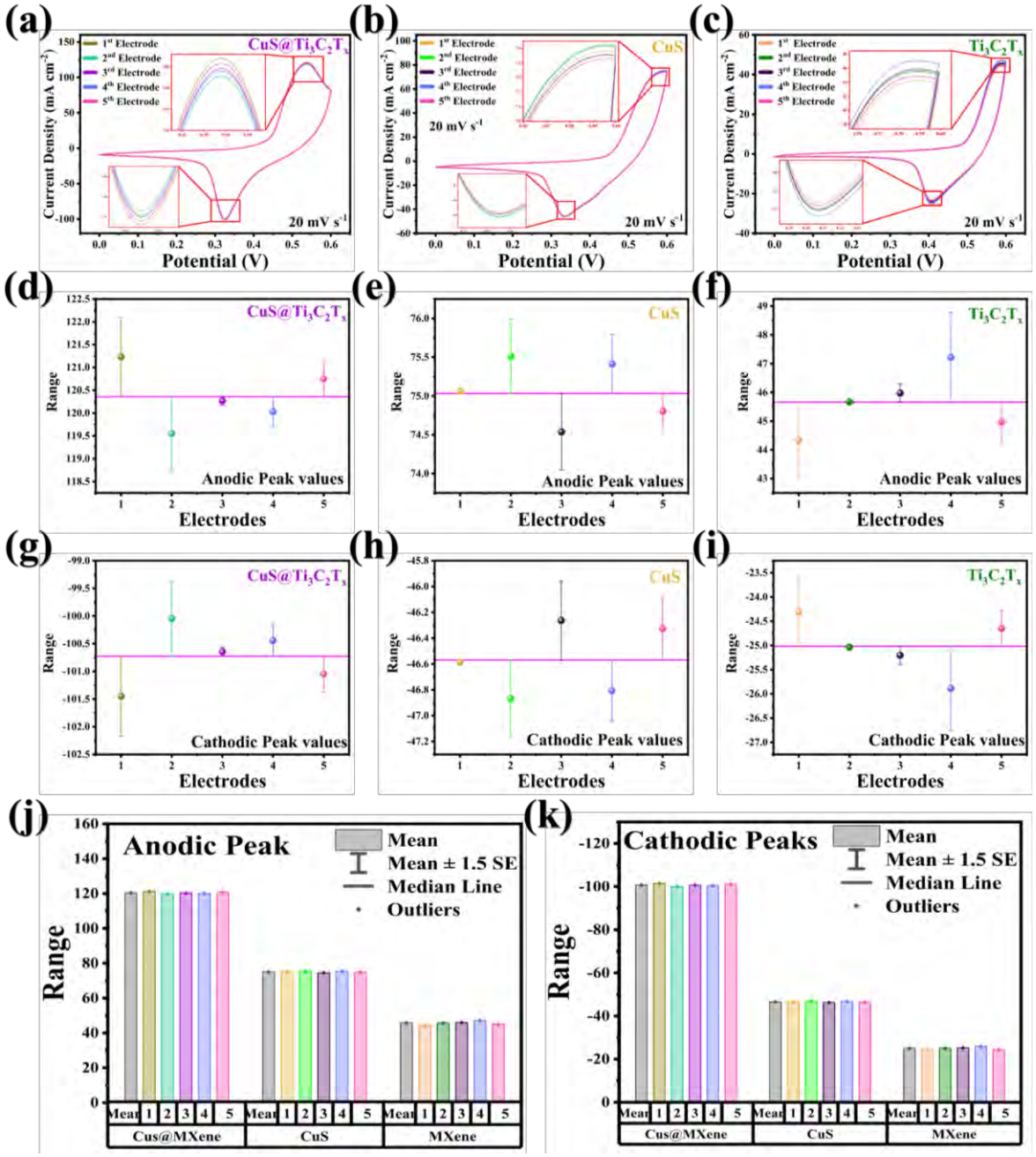

Figure S 5: CV curves for all replicates at 20 mV s^{-1} (a) CuS@$Ti_3C_2T_x$, (b) CuS and (c) $Ti_3C_2T_x$; Error bars for anodic peak currents (d) CuS@$Ti_3C_2T_x$, (e) CuS and (f) $Ti_3C_2T_x$; Error bars for cathodic peak currents (g) CuS@$Ti_3C_2T_x$, (h) CuS and (i) $Ti_3C_2T_x$; (j) comparison for standard deviations of anodic peak currents (k) comparison for standard deviations of cathodic peak currents.

To further analyze the results, galvanostatic charge-discharge (GCD) curves were obtained for each electrode type, with five replicates for each sample facilitating the calculation of specific capacitance and energy density represented in Figure S6.

Figure S6(a) displays the GCD curves for the five replicates of CuS@$Ti_3C_2T_x$, demonstrating highly consistent results with only minor variations attributable to factors such as human error or environmental influences. Figure S6(d) illustrates error bars for the energy density values, with the mean indicated by a magenta line. The results for the third electrode closely align with this mean. Figure S6(b) presents the GCD curves for the five replicates of CuS, revealing a similar consistency among measurements. The error bars for energy density values are provided in Figure S6(e), again with the mean marked by a magenta line. The results for the first electrode are in close agreement with this mean. In Figure S6(c), the GCD curves for $Ti_3C_2T_x$ reinforce the reliability of the measurements, with error bars for energy density values shown in Figure S6(f), where the mean is indicated by a magenta line. Results from the second electrode closely align with this mean.

Furthermore, Figure S6(g) summarizes the standard deviations of specific capacitance values across all samples. CuS@$Ti_3C_2T_x$ exhibits a standard deviation of 5.4608, with a relative standard deviation of 0.5699%. For CuS, the standard deviation is 4.8230, leading to a relative standard deviation of 0.6588%, while $Ti_3C_2T_x$ shows a standard deviation of 12.3462 and a relative standard deviation of 3.2852%.

These comprehensive results highlight the consistency and reliability of our electrochemical measurements across the various tested electrodes. Additional statistical calculations related to peak current values, specific capacitance, and energy density are included in the accompanying table for further reference.

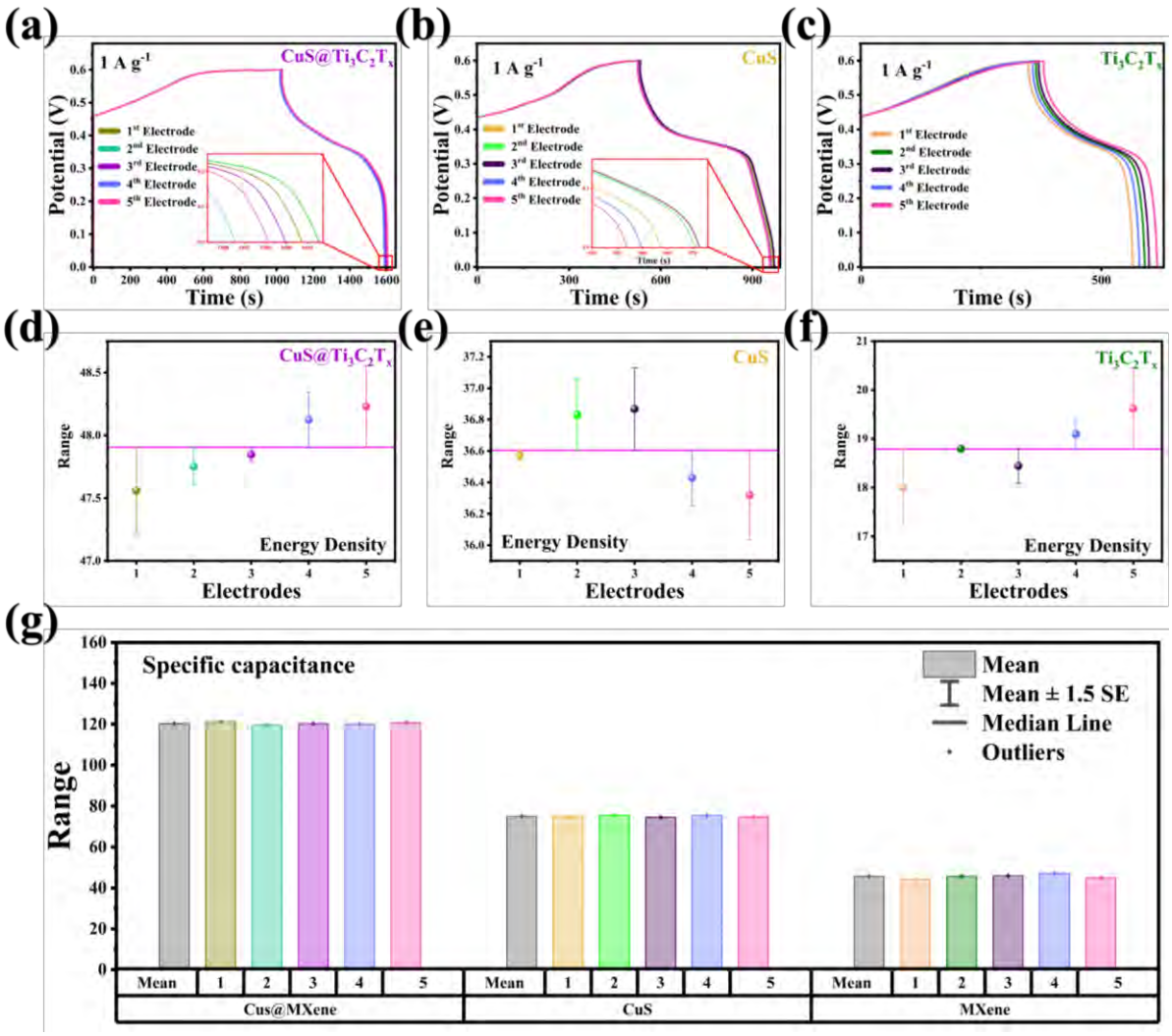

Figure S 6: GCD curves for all replicates at 1 A g^{-1} (a) CuS@$Ti_3C_2T_x$, (b) CuS and (c) $Ti_3C_2T_x$; Error bars for Energy density (d) CuS@$Ti_3C_2T_x$, (e) CuS and (f) $Ti_3C_2T_x$; (j) comparison of standard deviation for specific capacitance.

CuS@$Ti_3C_2T_x$							
	Mean	**Standard Deviation**	**Variance**	**Mean Absolute Deviation (MAD)**	**Standard Error of Mean**	**Coefficient of variance CV**	**Relative Standard Deviation RSD**
Anodic Peak Current	120.367173	0.648488282	0.42053705	0.49955776	0.2900128	0.0053876	0.54%
Cathodic Peak Current	-100.72506	0.54266476	0.29448504	0.418037456	0.2426871	-0.005388	-0.54%
Specific Capacitance	958.058242	5.46080981	29.8204438	4.3852623	2.4421484	0.0056999	0.57%
Energy Density	47.9029121	0.27304049	0.07455111	0.074551109	0.1221074	0.0056999	0.57%

CuS							
	Mean	**Standard Deviation**	**Variance**	**Mean Absolute Deviation (MAD)**	**Standard Error of Mean**	**Coefficient of variance CV**	**Relative Standard Deviation RSD**
Anodic Peak Current	75.0320988	0.43888946	0.192623958	0.354043082	0.19627733	0.00584936	0.58%
Cathodic Peak Current	-46.570477	0.272407303	0.074205739	0.219745357	0.121824249	-0.0058494	-0.58%
Specific Capacitance	732.088793	4.823	23.2613872	3.91324842	2.156913	0.006588	0.66%
Energy Density	36.6044396	0.2411503	0.05815346	0.19566241	0.107845	0.006588	0.66%

$Ti_3C_2T_x$							
	Mean	**Standard Deviation**	**Variance**	**Mean Absolute Deviation (MAD)**	**Standard Error of Mean**	**Coefficient of variance CV**	**Relative Standard Deviation RSD**
Anodic Peak Current	45.6332134	1.09085351	1.18996138	0.784973832	0.48784452	0.02390481	2.39%
Cathodic Peak Current	-25.016128	0.598005907	0.357611065	0.430322664	0.26743637	-0.0239048	-2.39%
Specific Capacitance	375.808873	12.3462732	152.430461	9.0922248	5.5214212	0.0328525	3.29%
Energy Density	18.7904437	0.617313658	0.381076152	0.45461124	0.2760711	0.0328525	3.29%

S4.1. CV and GCD results:

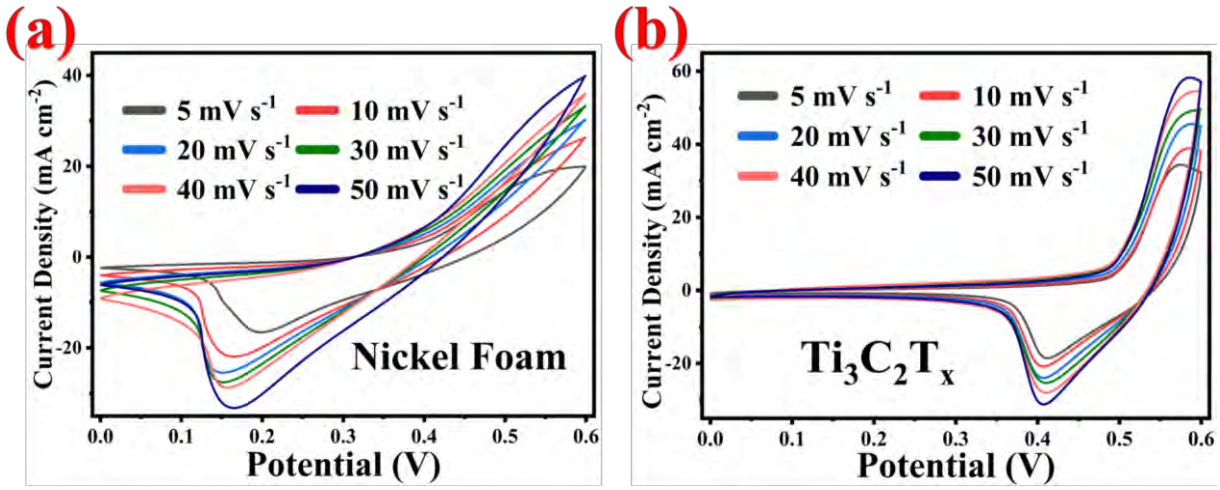

Figure S 7. Cyclic Voltammetry (CV) curves at scan rates ranging from 1 mV s^{-1} to 20 mV s^{-1} for (a) Nickel Foam, (b) $Ti_3C_2T_x$/MXene.

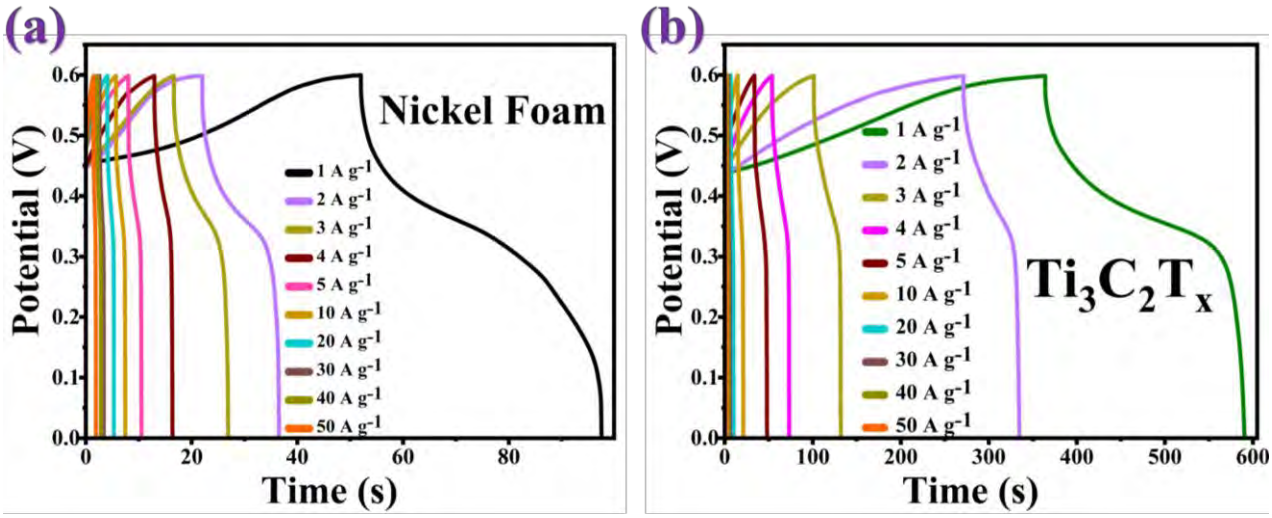

Figure S 8. GCD graph of (a) Nickel Foam, (b) $Ti_3C_2T_x$/MXene

S4.2. Energy Density For all synthesised electrodes:

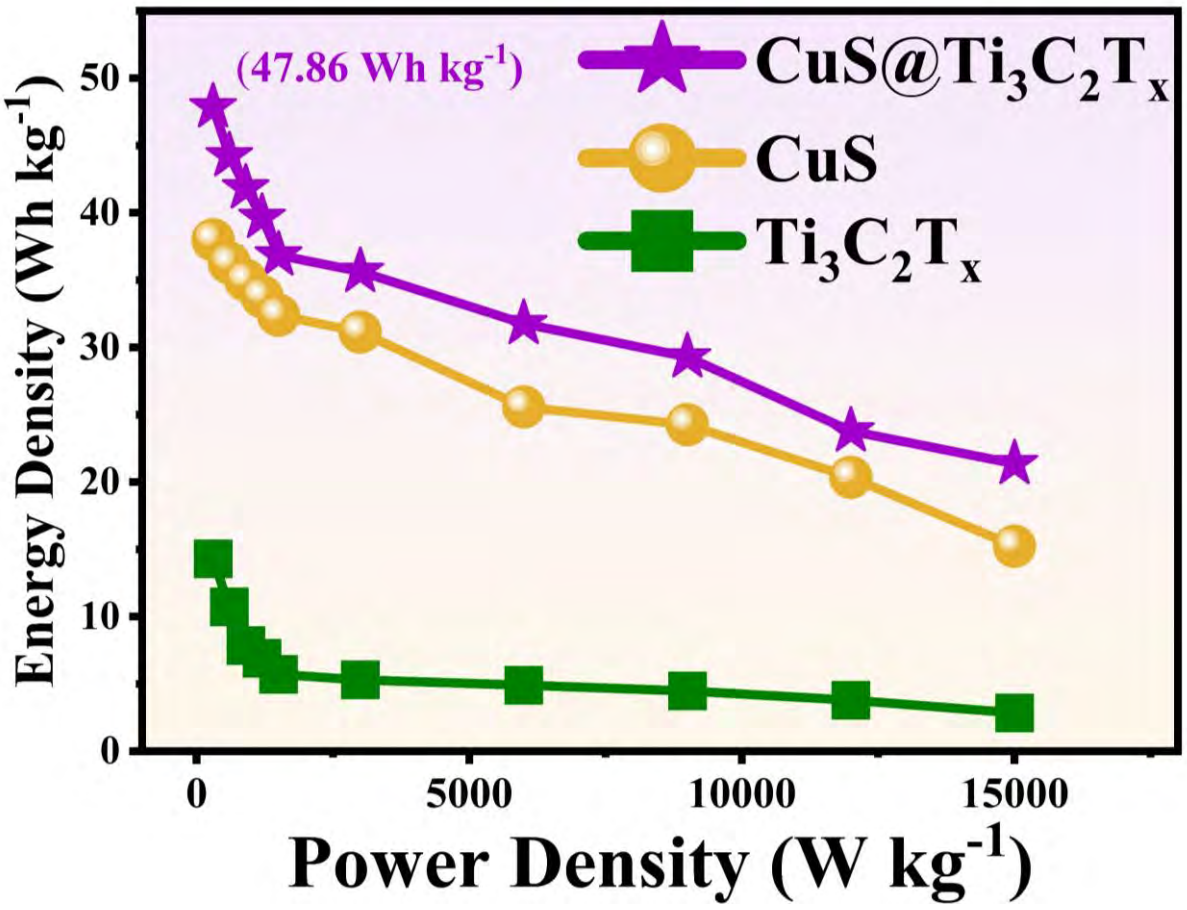

Figure S 9. Energy density vs power density diagram for synthesised electrodes.

Cyclic stability of CuS@$Ti_3C_2T_x$/MXene after 10,000 GCD cycles:

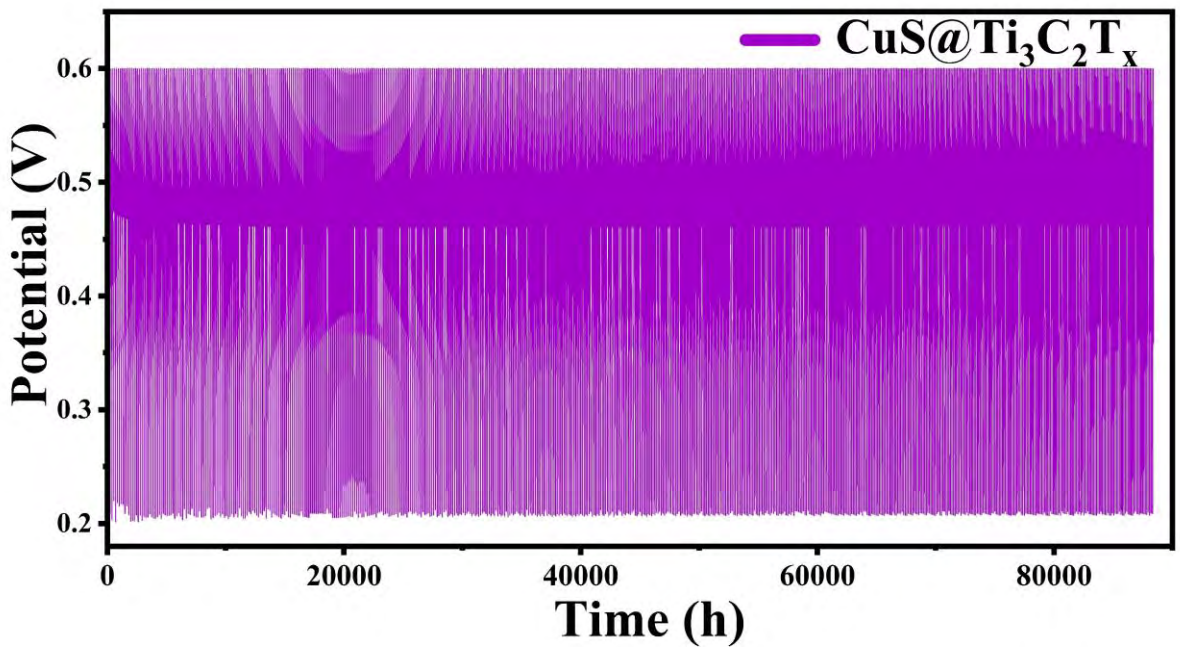

S4.3. Bode Plot:

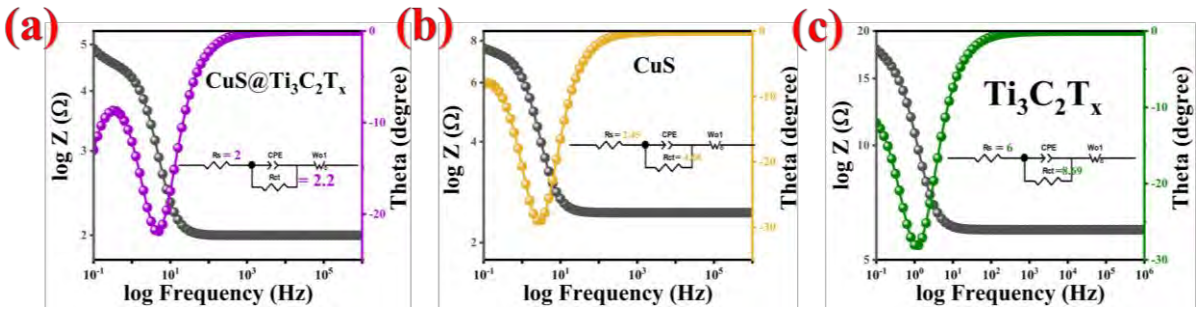

Figure S 10. Bode Plots along with the equivalent circuits (a) CuS@$Ti_3C_2T_x$ (b) CuS and (c) $Ti_3C_2T_x$.

S4.4. CV GCD of Active Carbon:

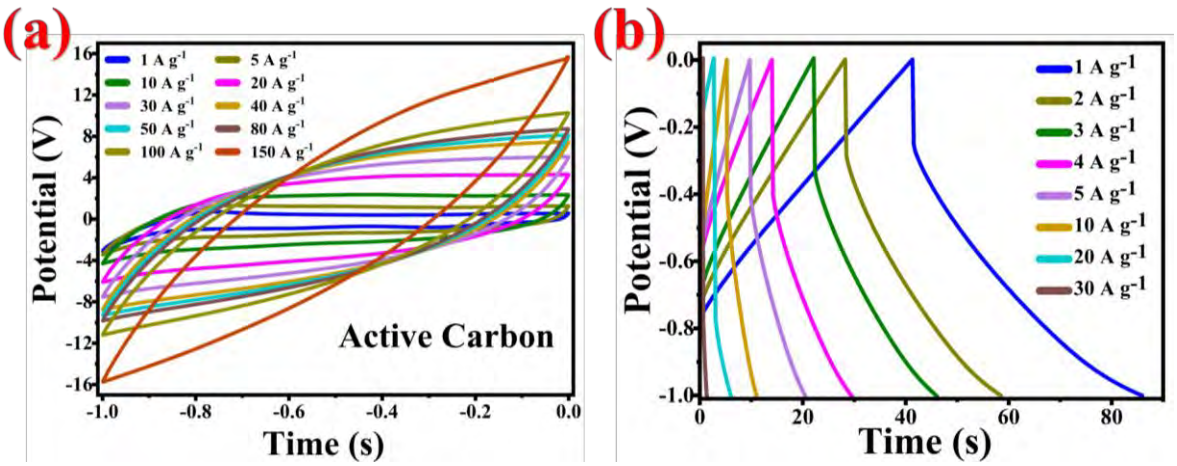

Figure S 11. CV and GCD plots of Active Carbon.

S4.5. Bode Plot:

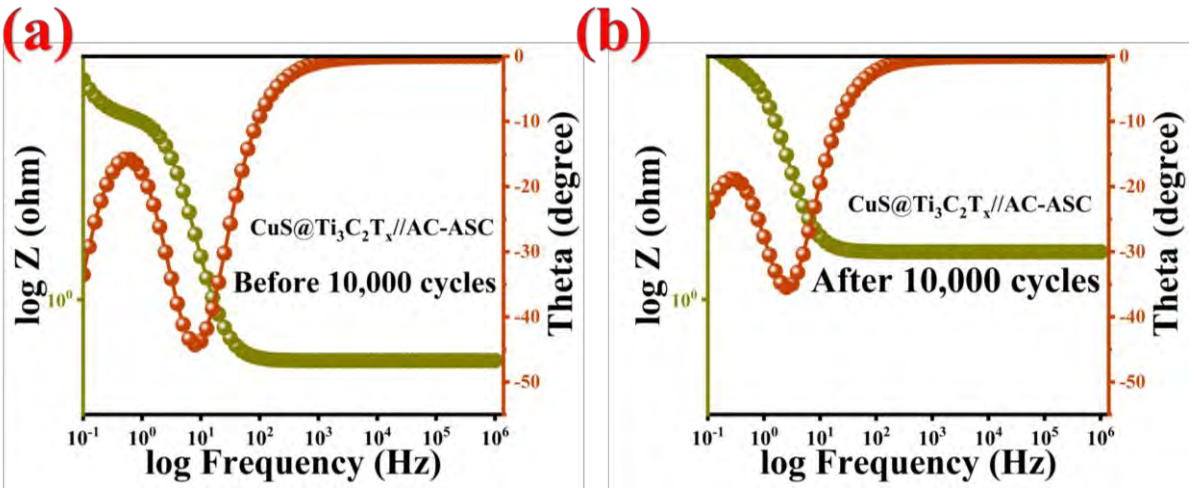

Figure S 12. Bode plot of CuS@$Ti_3C_2T_x$//AC-ASC before and after 10,000 cycles.

The Bode plot analysis reveals that the impedance increases and the capacitance decreases as the cycling progresses. This increase in impedance leads to distortion in the impedance response, particularly at higher frequencies. Additionally, the logarithm of the impedance experiences a moderate reduction, accompanied by curvature distortion. These observations indicate the presence of pseudocapacitive behavior, as evidenced by the differences in phase angle.

Table S 1. Table or equivalent resistance before and after cyclic stability.

State of electrode	R_{ct}	R_p	R_w
Before 10000 cycles	0.65	2.5	0.4
After 10000 cycles	1.4	3.8	0.5

S5. Electrocatalytic Water-splitting:

Water electrolysis (H_2) and oxygen (O_2) on the cathode and anode accompanied with hydrogen evolution reaction (HER) and the oxygen evolution reaction (OER), respectively. The electrodes for water electrolysis were prepared with the same process as described earlier. All experimental tests were conducted in a 1 M potassium hydroxide (KOH) electrolyte solution.

S5.1 HER:

In the present study, the cathode material employed for the Hydrogen Evolution Reaction (HER) was CuS@$Ti_3C_2T_x$/MXene. The anode material consisted of a graphite rod, while the reference electrode utilized was Ag/AgCl. During the HER process, protons (H+) undergo adsorption onto the electrode surface. Subsequently, a Tafel reaction occurs at the electrode-electrolyte interface, leading to the evolution of hydrogen gas (H2).

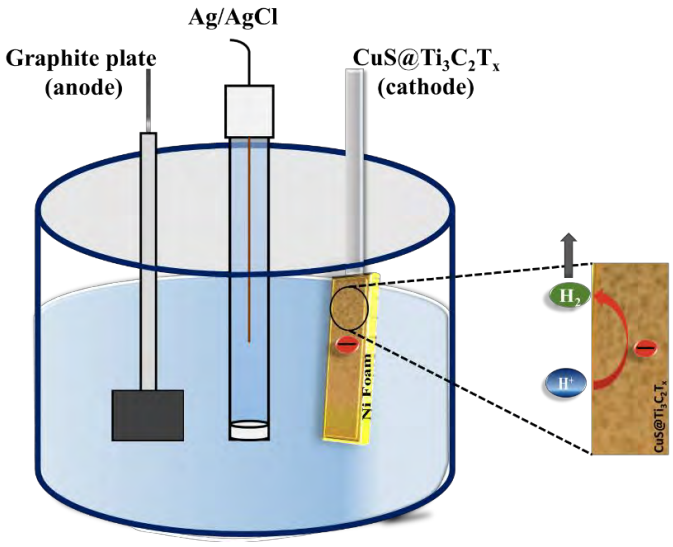

Figure S 13. Schematic illustration of 3 electrode system for using CuS@$Ti_3C_2T_x$/MXene as an electrocatalyst HER.

S5.2 OER:

In this study, we investigated the Oxygen Evolution Reaction (OER) with great attention to detail. As the anode material, we used CuS@Ti3C2Tx/MXene, which is known for its exceptional properties. The cathode was a graphite rod, and the reference electrode was the renowned Ag/AgCl configuration. During the OER process, an intriguing phenomenon occurs as hydroxide ions (OH-) adsorb onto the electrode surface, initiating a series of chemical reactions. At the electrode-electrolyte interface, a four-electron transfer process takes place, leading to the release of oxygen gas (O2) and water molecules (H2O). We conducted these tests to gain a deeper understanding of the OER mechanism and its potential applications in water splitting technologies.

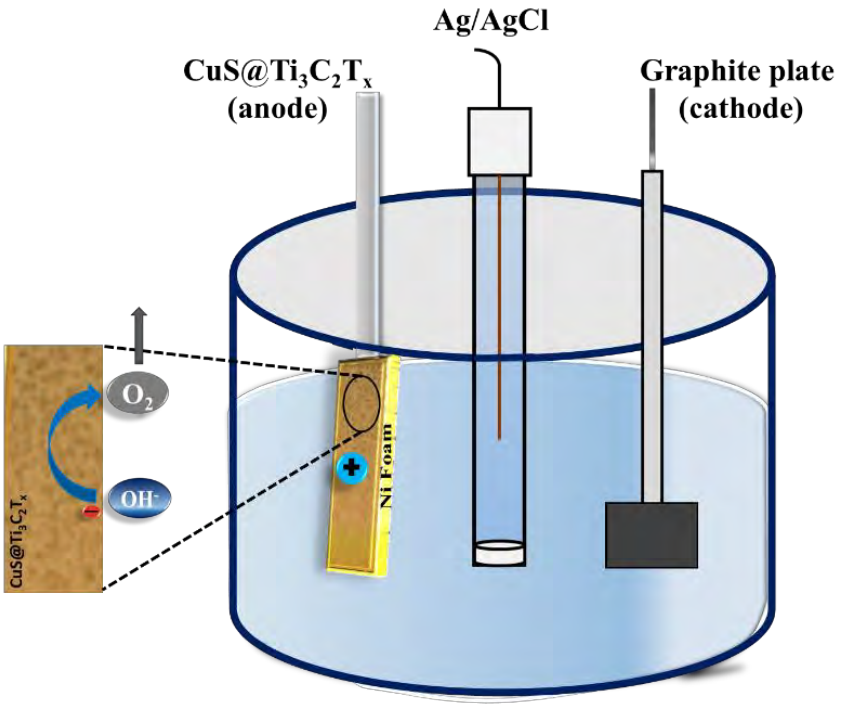

Figure S 14. Schematic illustration of 3 electrode system for using $CuS@Ti_3C_2T_x$/MXene as an electrocatalyst OER.

S5.3 Overall water splitting of CuS@$Ti_3C_2T_x$/MXene:

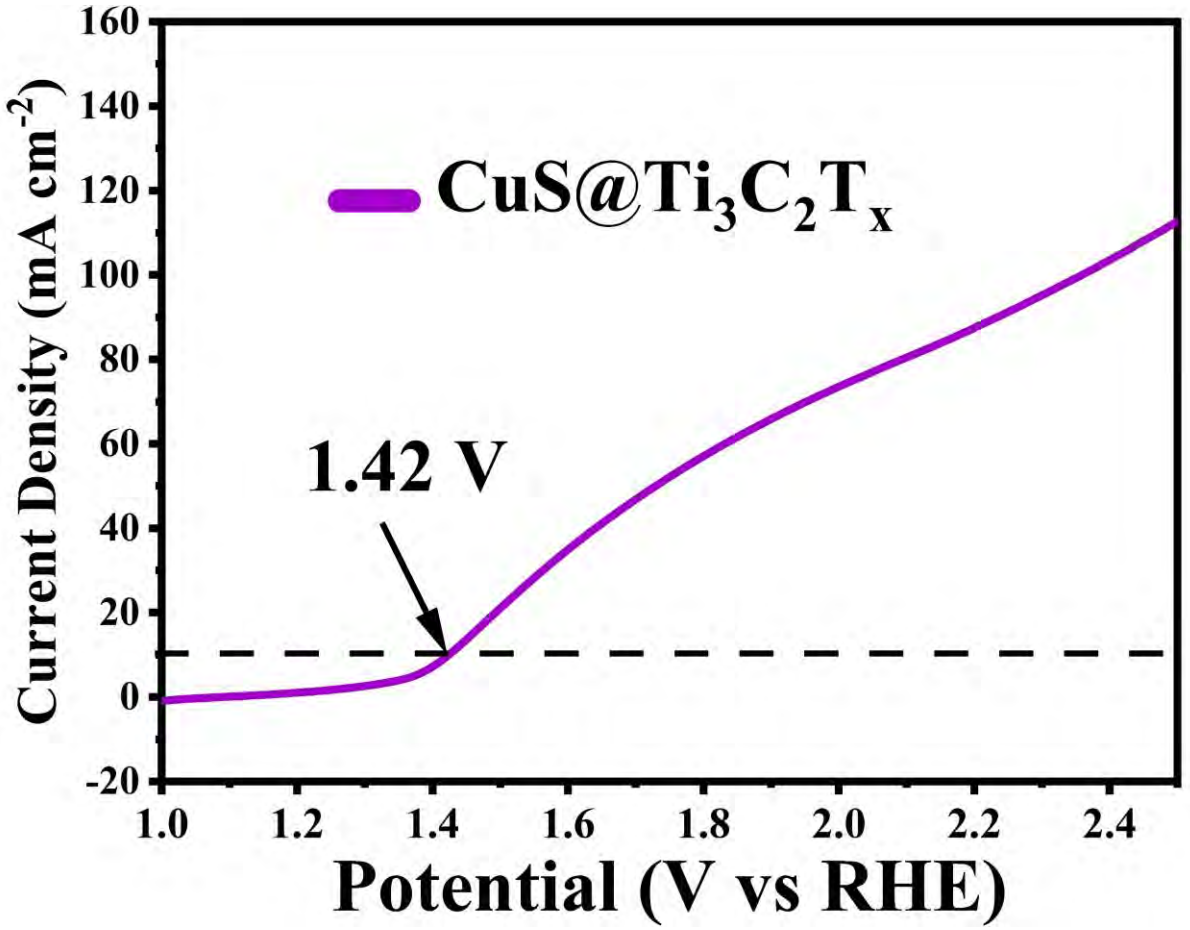

Figure S 15. Overall water splitting of CuS@Ti3C2Tx using alkaline electrolyte (1M KOH).

S6. Cyclic Stability comparison of MXene based electrodes:

Table S 2. Cycle stability comparison of various $Ti_3C_2T_x$/MXene -based electrode materials presented in literatures and this work.

Positive materials	**Voltage range (V)**	**Current Density ($A\ g^{-1}$)**	**Number of cycles**	**Capacitance retention (%)**	**Ref.**
CuS@$Ti_3C_2T_x$/MXene	**0~0.6**	**5**	**10000**	**99.1**	**This Work**
$NiCo_2Se_4$/MXene	0~0.4	5	3000	93.9	[12]
HS−NCS@MXene	0~0.6	20	10000	96	[13]
MXene@Ni-Mn LDH	0~0.5	6	5000	79.1	[14]
MXene@$CoSe_2$/Ni_3Se_4	0~0.5	5	10000	75	[15]
p-MXene/Ni_3S_4@CuS	0~0.45	15	30000	91.2	[16]
CoS@MXene/CF	0~0.45	10	10000	97.5	[17]

S7. Cyclic Stability comparison of MXene based ASCs deviceTable S 3. Cycle stability comparison of various $Ti_3C_2T_x$/MXene -based ASC devices.

MXene based devices	**Electrolyte**	**Potential window (V)**	**Specific capacitance**	**Current Density mA cm^{-2}**	**Energy density (Wh kg^{-1})**	**Power density (W kg^{-1})**	**Capacitance retention (%)**	**Number of cycles**	**Ref.**
AC//CuSe@ $Ti_3C_2T_x$/MXene	**7 M KOH**	**1.6**	**361.2 F g^{-1}**	**1 A g^{-1}**	**36.11**	**600**	**98.84**	**10000**	**This Work**
rGO//$Ti_3C_2T_x$	3 M H_2SO_4	1.8	76.5 F g^{-1}	1 A g^{-1}	34.4	1000	~100	10000	19
NiCo-MOF/$Ti_3C_2T_x$/AC	2 M KOH	1.5	126.4 F g^{-1}	0.5 A g^{-1}	39.5	562.5	82.3	10000	20
$NiCo_2S_4$/MXene//AC	KOH	1.7	171.2	1 A g^{-1}	68.7	850	89.5	5000	21
MXene/NCF//MXene/NCF	PVA/KOH	1.0	63 F g^{-1}	1 A g^{-1}	8.75	1871	96	2500	22
$Ti_3C_2T_x$/$CuCo_2S_4$//AC	6 M KOH	1.6	269.4 C g^{-1}	1 A g^{-1}	66.8	895.1	88.2	10000	23
rGO/CNT/PANI//$Ti_3C_2T_x$	3 M H_2SO_4	1.5	116.9	10 mV s^{-1}	28.6	590	80	10000	24

RuO_2//$Ti_3C_2T_x$	PVA-H_2SO_4	1.6	93 F g^{-1}	50 mV s^{-1}	29	3800	86	20000	25
$Ti_3C_2T_x$/NiS//G/AC	2 M KOH	1.5	56.73	1 A g^{-1}	17.69	750	97.7	3000	26
$MnCo_2S_4$/MXene//AC	3 M KOH	1.6	460 C g^{-1}	0.5 A g^{-1}	25.6	6400	100	12000	27
NiFe-LDH/$Ti_3C_2T_x$//AC	1 M KOH	1.3	135.7 F g^{-1}	1 A g^{-1}	42.4	758.27	86	1000	28

S8. HER and OER performance of electrocatalysts:

Table S 4. HER performance of CuS/$Ti_3C_2T_x$/MXene and several reported electrocatalysts.

Catalyst	**Morphology**	**Substrate**	**Electrolyte**	**Overpotential η (mV)**	**Current density (mA cm^{-2})**	**Ref.**
CuS@$Ti_3C_2T_x$	**Nanosheets Nanospheres**	**Ni Foam**	**1M KOH**	**89.7**	**10**	**This Work**
CuS	Nano spheres	Ni Foam	1M KOH	279	10	[18]

(CuS/Ti $_3C_2Cl_2$)	2D sheets	Ni Foam	1M KOH	163	10	[29]
MoS_2/Ni-Fe-LDH	Nano sheets	Ni Foam	1M KOH	300	10	[30]
NiPS3	Nano sheets	Ni Foam	1M KOH	530	10	[31]
MoOx/Ni_3S_2/Ni foam	Hollow microsphere	Ni Foam	1M KOH	200	15	[32]
MoS_2@CNF	Nano fiber	Ni Foam	1M KOH	186	10	[33]

Table S 5. OER performance of CuS/$Ti_3C_2T_x$/MXene and several reported electrocatalysts

Catalyst	**Morphology**	**Electrolyte**	**Overpotential η (mV)**	**Tafel Slope (mV dec^{-1})**	**Current density (mA cm^{-2})**	**Ref.**
CuS@$Ti_3C_2T_x$	**Nanosheets Nanospheres**	**1M KOH**	**171**	**39.3**	**30**	**This work**
$Ti_3C_2T_X$-FeOOH	Nano sheets	1M KOH	420	31.7	10	[34]

(CuS/$Ti_3C_2Cl_2$)	2D sheets	1M KOH	334	42	50	[29]
NiFe-LDH/$Ti_3C_2T_X$/NF	Nano sheets	1M KOH	229	44	10	[35]
FeS_2@$Ti_3C_2T_x$	Nano sheets	1M KOH	240	58.6	10	[36]
FeNi@$Mo_2TiC_2T_x$@NF	Hollow microsphere	1M KOH	195	42	10	[37]
$NiCo_2O_4$	3 D nano flowers	1M KOH	383	187	10	[38]

References:

[1]. Wang, Kaifeng, Yujie Chen, Ran Tian, Hua Li, Ying Zhou, Huanan Duan, and Hezhou Liu., Porous Co–C core–shell nanocomposites derived from Co-MOF-74 with enhanced electromagnetic wave absorption performance, ACS applied materials & interfaces. 10, 13 (2018) 11333-11342. https://doi.org/10.1021/acsami.8b00965

[2]. Kresse, Georg, and Jürgen Furthmüller., Efficiency of ab-initio total energy calculations for metals and semiconductors using a plane-wave basis set, Computational materials science. 6, 1 (1996) 15-50. https://doi.org/10.1016/0927-0256(96)00008-0

[3]. Kresse, Georg, and Jürgen Furthmüller., Efficient iterative schemes for ab initio total-energy calculations using a plane-wave basis set, Physical review B. 54, 16 (1996): 11169. https://doi.org/10.1103/PhysRevB.54.11169

[4]. Kresse, Georg, and Daniel Joubert., From ultrasoft pseudopotentials to the projector augmented-wave method, Physical review b. 59, 3 (1999) 1758. https://doi.org/10.1103/PhysRevB.59.1758

[5]. Perdew, John P., Kieron Burke, and Matthias Ernzerhof., Generalized gradient approximation made simple, Physical review letters. 77, 18 (1996) 3865. https://doi.org/10.1103/PhysRevLett.77.3865

[6]. Heydari, Hamid, Seyyed Ebrahim Moosavifard, Saeed Elyasi, and Mohammad Shahraki., Nanoporous CuS nano-hollow spheres as advanced material for high-performance supercapacitors, Applied Surface Science. 394 (2017) 425-430. https://doi.org/10.1016/j.apsusc.2016.10.138

[7]. Li, Caixia, Ping He, Lingpu Jia, Xingquan Zhang, Tinghong Zhang, Faqin Dong, Mingqian He et al., Facile synthesis of 3D CuS micro-flowers grown on porous activated carbon derived from pomelo peel as electrode for high-performance supercapacitors, Electrochimica Acta. 299 (2019) 253-261. https://doi.org/10.1016/j.electacta.2019.01.004

[8]. Yue, Congmei, Hougui Li, Hongwei Shi, Aifeng Liu, Zengcai Guo, Jingbo Mu, Xiaoliang Zhang, Xiaoyan Liu, and Hongwei Che., Ag nanoparticles decorated CuS sub-micron flowers with enhanced energy storage performance for hybrid supercapacitors, Journal of Alloys and Compounds. 885 (2021) 161080. https://doi.org/10.1016/j.jallcom.2021.161080

[9]. El-Hout, Soliman I., Saad G. Mohamed, Amira Gaber, Sayed Y. Attia, Ahmed Shawky, and Said M. El-Sheikh., High electrochemical performance of rGO anchored CuS

nanospheres for supercapacitor applications, Journal of Energy Storage. 34 (2021) 102001. https://doi.org/10.1016/j.est.2020.102001

[10]. Naveed, Muhammad, Waqar Younas, Youqi Zhu, Souleymen Rafai, Quanqing Zhao, Muhammad Tahir, Nouraiz Mushtaq, and Chuanbao Cao., Template free and facile microwave-assisted synthesis method to prepare mesoporous copper sulfide nanosheets for high-performance hybrid supercapacitor, Electrochimica Acta. 319 (2019) 49-60. https://doi.org/10.1016/j.electacta.2019.06.169

[11]. Huang, Ke-Jing, Ji-Zong Zhang, Yang Liu, and Yan-Ming Liu., Synthesis of reduced graphene oxide wrapped-copper sulfide hollow spheres as electrode material for supercapacitor, International Journal of Hydrogen Energy. 40, 32 (2015) 10158-10167. https://doi.org/10.1016/j.ijhydene.2015.05.152

[12]. Liu, Yuxing, Jiaxu Gong, Jiaheng Wang, Cunhai Hu, Mingzhen Xie, Xiaoli Jin, Shuai Wang, and Yatang Dai., Facile fabrication of MXene supported nickel-cobalt selenide ternary composite via one-step hydrothermal for high-performance asymmetric supercapacitors, Journal of Alloys and Compounds. 899 (2022) 163354. https://doi.org/10.1016/j.jallcom.2021.163354

[13]. Javed, Muhammad Sufyan, Xiaofeng Zhang, Salamat Ali, Abdul Mateen, Muhammad Idrees, Muhammad Sajjad, Saima Batool et al., Heterostructured bimetallic–sulfide@ layered $Ti_3C_2T_x$–MXene as a synergistic electrode to realize high-energy-density aqueous hybrid-supercapacitor, Nano Energy. 101 (2022) 107624. https://doi.org/10.1016/j.nanoen.2022.107624

[14]. Wang, Wandi, Demin Jiang, Xing Chen, Kun Xie, Yinhua Jiang, and Yuqiao Wang., A sandwich-like nano-micro LDH-MXene-LDH for high-performance supercapacitors, Applied Surface Science. 515 (2020) 145982. https://doi.org/10.1016/j.apsusc.2020.145982

[15]. Yang, Yuan, Xiaoyu Huang, Congyi Sheng, Yaoyao Pan, Yin Huang, and Xiuhua Wang., In-situ formation of MOFs derivatives $CoSe_2/Ni_3Se_4$ nanosheets on MXene nanosheets for hybrid supercapacitor with enhanced electrochemical performance, Journal of Alloys and Compounds. 920 (2022) 165908. https://doi.org/10.1016/j.jallcom.2022.165908

[16]. Guo, Hao, Junye Zhang, Fan Yang, Mingyue Wang, Tingting Zhang, Yanrui Hao, and Wu Yang., Sandwich-like porous MXene/Ni_3S_4/CuS derived from MOFs as superior supercapacitor electrode, Journal of Alloys and Compounds. 906 (2022) 163863. https://doi.org/10.1016/j.jallcom.2022.163863

[17]. Liao, Leiping, Aitang Zhang, Kun Zheng, Rui Liu, Yujun Cheng, Lihua Wang, Aihua Li, and Jingquan Liu., Fabrication of cobaltous sulfide nanoparticle-modified 3D MXene/carbon foam hybrid aerogels for all-solid-state supercapacitors, ACS Applied Materials & Interfaces. 13, 24 (2021) 28222-28230. https://doi.org/10.1021/acsami.1c05904

[18]. Shi, Guodong, Zixiong Fan, Lili Du, Xinliang Fu, Changming Dong, Wei Xie, Dongbing Zhao, Mei Wang, and Mingjian Yuan., In situ construction of graphdiyne/CuS heterostructures for efficient hydrogen evolution reaction, Materials Chemistry Frontiers. 3, 5 (2019) 821-828. https://doi.org/10.1039/C9QM00064J

[19]. Li, Mai, Zheyi Meng, Ruichao Feng, Kailan Zhu, Fengfeng Zhao, Chunrui Wang, Jiale Wang, Lianwei Wang, and Paul K. Chu., Fabrication of bimetallic oxides (MCo2O4: M= Cu, Mn) on ordered microchannel electro-conductive plate for high-performance hybrid supercapacitors, Sustainability 13. 17 (2021) 9896. https://doi.org/10.3390/su13179896

[20]. Wang, Yanzhong, Yuexin Liu, Chao Wang, Hu Liu, Jiaoxia Zhang, Jing Lin, Jincheng Fan, Tao Ding, Jong E. Ryu, and Zhanhu Guo., Significantly enhanced ultrathin NiCo-based MOF nanosheet electrodes hybrided with Ti3C2Tx MXene for high performance

asymmetric supercapacitor, Engineered Science 9. 12 (2020) 50-59. http://dx.doi.org/10.30919/es8d903

[21]. Fu, Jianjian, Lei Li, Je Moon Yun, Damin Lee, Bong Ki Ryu, and Kwang Ho Kim., Two-dimensional titanium carbide (MXene)-wrapped sisal-Like NiCo2S4 as positive electrode for High-performance hybrid pouch-type asymmetric supercapacitor, Chemical Engineering Journal. 375 (2019) 121939. https://doi.org/10.1016/j.cej.2019.121939

[22]. Sun, Li, Gongsheng Song, Yafei Sun, Qiang Fu, and Chunxu Pan., MXene/N-doped carbon foam with three-dimensional hollow neuron-like architecture for freestanding, highly compressible all solid-state supercapacitors, ACS Applied Materials & Interfaces. 12, 40 (2020) 44777-44788. https://doi.org/10.1021/acsami.0c13059

[23]. X. Chen, Z. Ding, H. Yu, H. Ge, W. Liu, S. Sun, Facile fabrication of CuCo2S4 nanoparticles/MXene composite as anode for high-performance asymmetric supercapacitor. Mater. Chem. Front. 5 (2021) 7606-7616. https://doi.org/10.1039/D1QM01029H

[24]. Li, Ke, Xuehang Wang, Xiaofeng Wang, Meiying Liang, Valeria Nicolosi, Yuxi Xu, and Yury Gogotsi., All-pseudocapacitive asymmetric MXene-carbon-conducting polymer supercapacitors, Nano Energy. 75 (2020) 104971. https://doi.org/10.1016/j.nanoen.2020.104971

[25]. Jiang, Qiu, Narendra Kurra, Mohamed Alhabeb, Yury Gogotsi, and Husam N. Alshareef., All pseudocapacitive MXene-RuO2 asymmetric supercapacitors, Advanced Energy Materials. 8 13 (2018) 1703043. https://doi.org/10.1002/aenm.201703043

[26]. Liu, Hao, Rui Hu, Jiqiu Qi, Yanwei Sui, Yezeng He, Qingkun Meng, Fuxiang Wei, Yaojian Ren, and Yulong Zhao., A facile method for synthesizing NiS nanoflower grown on MXene (Ti3C2Tx) as positive electrodes for “supercapattery”, Electrochimica Acta. 353 (2020) 136526. https://doi.org/10.1016/j.electacta.2020.136526

[27]. Nasrin, K., K. Subramani, M. Karnan, and M. Sathish., MnCo2S4–MXene: A novel hybrid electrode material for high performance long-life asymmetric supercapattery, Journal of Colloid and Interface Science. 600 (2021) 264-277. https://doi.org/10.1016/j.jcis.2021.05.037

[28]. H. Zhou, F. Wu, L. Fang, J. Hu, H. Luo, T. Guan, B. Hu, M. Zhou., Layered NiFe-LDH/MXene nanocomposite electrode for high-performance supercapacitor, Int. J. Hydrog. Energy. 45 (2020) 13080-13089. https://doi.org/10.1016/j.jcis.2021.05.037

[29]. Sarfraz, Bilal, Muhammad Taqi Mehran, Faisal Shahzad, Sajjad Hussain, Salman Raza Naqvi, Hassnain Abbas Khan, and Khalid Mahmood., Bifunctional CuS/Cl-terminated greener MXene electrocatalyst for efficient hydrogen production by water splitting, RSC advances. 13, 32 (2023) 22017-22028. https://doi.org/10.1039/D3RA02581K

[30]. Islam, Md Shahinul, Minho Kim, Xiaoyan Jin, Seung Mi Oh, Nam-Suk Lee, Hyungjun Kim, and Seong-Ju Hwang., Bifunctional 2D superlattice electrocatalysts of layered double hydroxide–transition metal dichalcogenide active for overall water splitting, ACS Energy Letters. 3, 4 (2018) 952-960. https://doi.org/10.1021/acsenergylett.8b00134

[31]. Du, Cheng-Feng, Qinghua Liang, Raksha Dangol, Jin Zhao, Hao Ren, Srinivasan Madhavi, and Qingyu Yan., Layered tri-chalcogenido-phosphate: a new catalyst family for water splitting, Nano-micro letters. 10 (2018) 1-15. https://link.springer.com/article/10.1007/s40820-018-0220-6

[32]. Wu, Yuanyuan, Guo-Dong Li, Yipu Liu, Lan Yang, Xinran Lian, Tewodros Asefa, and Xiaoxin Zou., Overall water splitting catalyzed efficiently by an ultrathin nanosheet-built, hollow Ni3S2-based electrocatalyst, Advanced functional materials. 26, 27 (2016) 4839-4847. https://doi.org/10.1002/adfm.201601315

[33]. Khan, Muhammad Awais, Muhammad Taqi Mehran, Salman Raza Naqvi, Asif Hussain Khoja, Faisal Shahzad, Umair Sikander, Sajjad Hussain, Ramsha Khan, Bilal Sarfaraz, and

Mutawara Mahmood Baig., Reutilizing methane reforming spent catalysts as efficient overall water-splitting electrocatalysts, ACS omega. 6, 33 (2021) 21316-21326. https://doi.org/10.1021/acsomega.1c01558

[34]. Ibrahim, Kassa Belay, Tofik Ahmed Shifa, Sandro Zorzi, Marshet Getaye Sendeku, Elisa Moretti, and Alberto Vomiero., Emerging 2D materials beyond mxenes and TMDs: Transition metal carbo-chalcogenides, Progress in Materials Science. (2024) 101287. https://doi.org/10.1016/j.pmatsci.2024.101287

[35]. Yu, Mengzhou, Zhiyu Wang, Junshan Liu, Fu Sun, Pengju Yang, and Jieshan Qiu., A hierarchically porous and hydrophilic 3D nickel–iron/MXene electrode for accelerating oxygen and hydrogen evolution at high current densities, Nano Energy. 63 (2019) 103880. https://doi.org/10.1016/j.nanoen.2019.103880

[36]. Xie, Yaoyi, Hanzhi Yu, Liming Deng, R. S. Amin, Deshuang Yu, Amani E. Fetohi, Maxim Yu Maximov, Linlin Li, K. M. El-Khatib, and Shengjie Peng., Anchoring stable FeS 2 nanoparticles on MXene nanosheets via interface engineering for efficient water splitting, Inorganic Chemistry Frontiers. 9, 4 (2022) 662-669. https://doi.org/10.1039/D1QI01465J

[37]. Wang, Jiayang, Peilei He, Yongli Shen, Linxiu Dai, Zhe Li, Yue Wu, and Changhua An., FeNi nanoparticles on $Mo_2Ti_3C_2T_x$MXene@nickel foam as robust electrocatalysts for overall water splitting, Nano Research. 14 (2021) 3474-3481. https://link.springer.com/article/10.1007/s12274-021-3660-0

[38]. Li, Zesheng, Bolin Li, Jiaming Chen, Qi Pang, and Peikang Shen., Spinel $NiCo_2O_4$ 3-D nanoflowers supported on graphene nanosheets as efficient electrocatalyst for oxygen evolution reaction, International Journal of Hydrogen Energy. 44, 31 (2019) 16120-16131. https://doi.org/10.1016/j.ijhydene.2019.04.219